Eur. Phys. J. C (2022) 82:915
https://doi.org/10.1140/epjc/s10052-022-10893-x

THE EUROPEAN PHYSICAL JOURNAL C

Regular Article - Theoretical Physics

Muon and electron $g-2$ anomalies in a flavor conserving 2HDM with an oblique view on the CDF M_W value

Francisco J. Botella[1,a], **Fernando Cornet-Gomez**[1,2,b], **Carlos Miró**[1,c], **Miguel Nebot**[1,d]

[1] Departament de Física Teòrica and Instituto de Física Corpuscular (IFIC), Universitat de València-CSIC, 46100 Burjassot, Spain
[2] Physics Department and Center for Education and Research in Cosmology and Astrophysics (CERCA), Case Western Reserve University, Cleveland, OH 44106, USA

Received: 1 September 2022 / Accepted: 7 October 2022 / Published online: 14 October 2022

Abstract We consider a type I or type X two Higgs doublets model with a modified lepton sector. The generalized lepton sector is also flavor conserving but with the new Yukawa couplings completely decoupled from lepton mass proportionality. The model is one loop stable under renormalization group evolution and it allows to reproduce the $g-2$ muon anomaly together with the different scenarios one can consider for the electron $g-2$ anomaly, related to the Cesium and/or to the Rubidium recoil measurements of the fine structure constant. Thorough parameter space analyses are performed to constrain all the model parameters in the different scenarios, either including or not including the recent CDF measurement of the W boson mass. For light new scalars with masses in the 0.2–1.0 TeV range, the muon anomaly receives dominant one loop contributions; it is for heavy new scalars with masses above 1.2 TeV that two loop Barr–Zee diagrams are needed. The electron $g-2$ anomaly, if any, must always be obtained with the two loop contributions. The final allowed regions are quite sensitive to the assumptions about perturbativity of Yukawa couplings, which influence unexpected observables like the allowed scalar mass ranges. On that respect, intermediate scalar masses, highly constrained by direct LHC searches, are allowed provided that the new lepton Yukawa couplings are fully scrutinized, including values up to 250 GeV. In the framework of a complete model, fully numerically analysed, we show the implications of the recent M_W measurement.

1 Introduction

In the search of Physics beyond the Standard Model (SM), disagreement between measurements and theoretical expectations, that is "anomalies", can play the role of beacons to guide our explorations. One longstanding anomaly concerns the anomalous magnetic moment of the muon $a_\mu = \frac{g_\mu - 2}{2}$. The *Muon g-2* experiment at Brookhaven [1] and its successor at Fermilab [2,3] have produced the following result

$$\delta a_\mu^{\text{Exp}} = a_\mu^{\text{Exp}} - a_\mu^{\text{SM}} = (2.5 \pm 0.6) \times 10^{-9}. \tag{1}$$

where a_μ^{Exp} is the experimental observation and a_μ^{SM} the SM theoretical expectation [4–24]. Although there are unsettled discrepancies concerning Hadronic Vacuum Polarization (HVP) contributions to a_μ^{SM} [25–27], we interpret $\delta a_\mu^{\text{Exp}}$ in Eq. (1) as a signal of New Physics (NP).[1]

Besides the muon, recent results concerning the anomalous magnetic moment of the electron might also be interpreted as NP hints [32]. On the one hand, perturbative calculations of $a_e = \frac{g_e - 2}{2}$, which have reached impressive levels [5,33–36], yield a_e^{SM} as a series in powers of the fine structure constant α. On the other hand, we have precise measurements of a_e^{Exp} such as [37]. In the past, such measurements were indeed used to infer values of α. On the contrary, measurements of atomic recoils [38] provide now more precise determinations of α, which give values of a_e^{SM} such that

$$\delta a_e^{\text{Exp,Cs}} = -(8.7 \pm 3.6) \times 10^{-13}\,, \tag{2}$$

from measurements with ^{133}Cs [39], and

$$\delta a_e^{\text{Exp,Rb}} = (4.8 \pm 3.0) \times 10^{-13}\,, \tag{3}$$

[1] Solving the anomaly in Eq. (1) by enhancing the HVP contribution could generate other tensions in electroweak precision fits [28–31].

[a] e-mail: Francisco.J.Botella@uv.es
[b] e-mail: Fernando.CornetGomez@case.edu (corresponding author)
[c] e-mail: Carlos.Miro@uv.es
[d] e-mail: Miguel.Nebot@uv.es

from measurements with ^{87}Rb [40].

In reference [41] the possibility to explain the values of $\delta a_\mu^{\rm Exp}$ from the *Muon g-2* Brookhaven experiment [1] together with $\delta a_e^{\rm Exp,Cs}$ in Eq. (2) was successfully addressed within a subclass of Two Higgs Doublets Models (2HDMs) with general flavor conservation [42,43]. This was achieved, of course, without conflicting with a large set of high and low energy constraints. The specific model considered, the so-called I-gℓFC 2HDM is a 2HDM without tree level scalar flavor changing neutral couplings (SFCNC): in the quark sector it is a type I 2HDM while in the lepton sector it is a general flavor conserving model. The existence of these two anomalies has been addressed in a variety of scenarios, including models with extra Higgs doublets [44–62], models with other scalar extensions [63–73] and supersymmetric models [74–78]. There are also plenty of studies with other approaches such as leptoquarks, vector-like fermions or extra gauge bosons, among others [79–95].

The present work extends and improves several aspects of [41].

- An improved numerical exploration of the parameter space shows that some unexpected regions of interest can be appropriately covered.
- Some theoretical assumptions like the perturbativity limits on Yukawa couplings had a significant impact on the analysis and were not fully considered.
- The latest *Muon g-2* Fermilab result [2,3] consolidates the need of NP brought by the previous Brookhaven result.
- For $a_e^{\rm Exp}$ the situation is rather unclear: within the present scenario, accommodating the values in Eq. (2) or in Eq. (3) may have non-trivial consequences in the model, since they differ in size and in sign.
- The recent measurement of the W boson mass by the CDF collaboration [96], which disagrees with SM expectations [97], can also be addressed in this context.

All in all, we are entering an era of exclusion or discovery at the LHC and improved analyses of such potential NP hints are necessary.

The manuscript is organized as follows. In Sect. 2, the model is presented. Section 3 is devoted to a discussion of general constraints which apply regardless of δa_ℓ. The new contributions to δa_ℓ are analysed in Sect. 4. The main aspects of the numerical analysis are introduced in Sect. 5. Next, Sect. 6 contains the results of the different analyses together with the corresponding discussions. Finally, the conclusions are presented in Sect. 7. We relegate to the appendices some aspects concerning different sections.

2 Model

The 2HDM is based on the SM gauge group with identical fermion matter content[2] and an additional complex scalar doublet. Hence, we have Φ_j $(j = 1, 2)$ and their corresponding C-conjugate fields defined as $\tilde{\Phi}_j \equiv i\sigma_2\Phi_j^*$, with opposite sign hypercharge.

The most general scalar potential of 2HDMs can be written as

$$\begin{aligned}\mathscr{V}(\Phi_1,\Phi_2) = {} & \mu_{11}^2\Phi_1^\dagger\Phi_1 + \mu_{22}^2\Phi_2^\dagger\Phi_2 + (\mu_{12}^2\Phi_1^\dagger\Phi_2 + \text{H.c.}) \\ & + \lambda_1(\Phi_1^\dagger\Phi_1)^2 + \lambda_2(\Phi_2^\dagger\Phi_2)^2 \\ & + 2\lambda_3(\Phi_1^\dagger\Phi_1)(\Phi_2^\dagger\Phi_2) + 2\lambda_4(\Phi_1^\dagger\Phi_2)(\Phi_2^\dagger\Phi_1) \\ & + [\lambda_5(\Phi_1^\dagger\Phi_2)^2 + \text{H.c.}] \\ & + [\lambda_6(\Phi_1^\dagger\Phi_1)(\Phi_1^\dagger\Phi_2) \\ & + \lambda_7(\Phi_2^\dagger\Phi_2)(\Phi_1^\dagger\Phi_2) + \text{H.c.}]\,,\end{aligned} \tag{4}$$

with real μ_{11}^2, μ_{22}^2 and λ_i $(i = 1$ to $4)$, whereas μ_{12}^2 and λ_j $(j = 5$ to $7)$ are complex in general. We assume that $\mathscr{V}(\langle\Phi_1\rangle, \langle\Phi_2\rangle)$ has an appropriate minimum at

$$\langle 0|\Phi_j|0\rangle = \frac{1}{\sqrt{2}}\begin{pmatrix}0\\ v_j e^{i\theta_j}\end{pmatrix}, \tag{5}$$

being θ_j and v_j $(v_j \geq 0)$ real numbers. Taking this into account, the Higgs doublets can be parametrized around the vacuum as

$$\Phi_j = e^{i\theta_j}\begin{pmatrix}\varphi_j^+\\ (v_j + \rho_j + i\eta_j)/\sqrt{2}\end{pmatrix}. \tag{6}$$

Introducing[3] $c_\beta \equiv \cos\beta \equiv v_1/v$, $s_\beta \equiv \sin\beta \equiv v_2/v$, $t_\beta \equiv \tan\beta = v_2/v_1$, with $\beta \in [0; \pi/2]$ and $v^2 = v_1^2 + v_2^2 = (\sqrt{2}G_F)^{-1} \simeq (246\ \text{GeV})^2$, one can perform a global $SU(2)$ rotation in the scalar space and express the scalar doublets in the so-called Higgs basis [98–100]

$$\begin{pmatrix}H_1\\ H_2\end{pmatrix} = \mathscr{R}_\beta\begin{pmatrix}e^{-i\theta_1}\Phi_1\\ e^{-i\theta_2}\Phi_2\end{pmatrix}, \quad \text{with}$$
$$\mathscr{R}_\beta = \begin{pmatrix}c_\beta & s_\beta\\ -s_\beta & c_\beta\end{pmatrix} \quad \text{and} \quad \mathscr{R}_\beta^T = \mathscr{R}_\beta^{-1}, \tag{7}$$

where only one linear combination of the scalar doublets, namely H_1, has a non-zero vacuum expectation value (vev):

$$\langle H_1\rangle = \frac{v}{\sqrt{2}}\begin{pmatrix}0\\ 1\end{pmatrix}, \quad \langle H_2\rangle = \begin{pmatrix}0\\ 0\end{pmatrix}. \tag{8}$$

The explicit degrees of freedom in this basis are defined by

$$H_1 = \begin{pmatrix}G^+\\ \frac{v+H^0+iG^0}{\sqrt{2}}\end{pmatrix}, \quad H_2 = \begin{pmatrix}\text{H}^+\\ \frac{R^0+iI^0}{\sqrt{2}}\end{pmatrix}, \tag{9}$$

[2] As in the SM, we do not include right-handed neutrinos.

[3] From now on, $t_\beta^{-1} = \cot\beta$.

where

$$\begin{pmatrix} G^+ \\ \mathrm{H}^+ \end{pmatrix} = \mathscr{R}_\beta \begin{pmatrix} \varphi_1^+ \\ \varphi_2^+ \end{pmatrix}, \quad \begin{pmatrix} H^0 \\ R^0 \end{pmatrix} = \mathscr{R}_\beta \begin{pmatrix} \rho_1 \\ \rho_2 \end{pmatrix}, \quad \begin{pmatrix} G^0 \\ I^0 \end{pmatrix} = \mathscr{R}_\beta \begin{pmatrix} \eta_1 \\ \eta_2 \end{pmatrix}. \tag{10}$$

As we can check, the would-be Goldstone bosons G^0 and $G^\pm$ get isolated as components of the first Higgs doublet. Likewise, we already identify two charged physical scalars $\mathrm{H}^\pm$ and three neutral fields $\{H^0, R^0, I^0\}$ that are not, in general, the mass eigenstates. The latter are determined by the scalar potential, which generates their mass matrix $\mathscr{M}_0^2$. This can be diagonalized by a 3×3 real orthogonal transformation, $\mathscr{R}$, as

$$\mathscr{R}^T \mathscr{M}_0^2 \mathscr{R} = \mathrm{diag}(m_\mathrm{h}^2, m_\mathrm{H}^2, m_\mathrm{A}^2), \quad \mathscr{R}^T = \mathscr{R}^{-1}, \tag{11}$$

and thus the physical scalars {h, H, A} are given by

$$\begin{pmatrix} \mathrm{h} \\ \mathrm{H} \\ \mathrm{A} \end{pmatrix} = \mathscr{R}^T \begin{pmatrix} H^0 \\ R^0 \\ I^0 \end{pmatrix}. \tag{12}$$

Neglecting CP violation in the scalar sector, one has

$$\mathscr{R} = \begin{pmatrix} s_{\alpha\beta} & -c_{\alpha\beta} & 0 \\ c_{\alpha\beta} & s_{\alpha\beta} & 0 \\ 0 & 0 & 1 \end{pmatrix}, \tag{13}$$

where $s_{\alpha\beta} \equiv \sin(\alpha+\beta)$ and $c_{\alpha\beta} \equiv \cos(\alpha+\beta)$, with $\pi/2-\alpha$ being the mixing angle that parametrizes the change of basis from the fields in Eq. (6) to the mass eigenstates in Eq. (12). We should point out that different conventions for Eq. (13) can be found in the literature.

Regarding the Yukawa sector, it is extended to

$$\begin{aligned} \mathscr{L}_\mathrm{Y} = & -\bar{Q}_L^0 \left(\Phi_1 Y_{d1} + \Phi_2 Y_{d2}\right) d_R^0 \\ & -\bar{Q}_L^0 \left(\tilde{\Phi}_1 Y_{u1} + \tilde{\Phi}_2 Y_{u2}\right) u_R^0 \\ & -\bar{L}_L^0 \left(\Phi_1 Y_{\ell 1} + \Phi_2 Y_{\ell 2}\right) \ell_R^0 + \mathrm{H.c.}\,, \end{aligned} \tag{14}$$

where the couplings Y_{dj}, Y_{uj} and $Y_{\ell j}$ $(j = 1, 2)$ are 3×3 complex matrices in flavor space. One should notice that there are only two flavor structures in the leptonic sector because we are not considering right-handed neutrinos. In the Higgs basis, the Yukawa Lagrangian takes the form

$$\begin{aligned} \mathscr{L}_\mathrm{Y} = & -\frac{\sqrt{2}}{v} \bar{Q}_L^0 \left(H_1 \mathrm{M}_d^0 + H_2 \mathrm{N}_d^0\right) d_R^0 \\ & -\frac{\sqrt{2}}{v} \bar{Q}_L^0 \left(\tilde{H}_1 \mathrm{M}_u^0 + \tilde{H}_2 \mathrm{N}_u^0\right) u_R^0 \\ & -\frac{\sqrt{2}}{v} \bar{L}_L^0 \left(H_1 \mathrm{M}_\ell^0 + H_2 \mathrm{N}_\ell^0\right) \ell_R^0 + \mathrm{H.c.}. \end{aligned} \tag{15}$$

It is then clear that the matrices M_f^0 $(f = d, u, \ell)$ are the non-diagonal fermion mass matrices since they are coupled to the only Higgs doublet that acquires a non-vanishing vev, i.e., H_1.

The model we are considering in the quark sector is defined by

$$Y_{d2} = d Y_{d1}\,, \quad Y_{u2} = d^* Y_{u1}\,, \tag{16}$$

which is equivalent to

$$\mathrm{N}_d^0 = t_\beta^{-1} \mathrm{M}_d^0\,, \quad \mathrm{N}_u^0 = t_\beta^{-1} \mathrm{M}_u^0\,. \tag{17}$$

In the leptonic sector, there exist two unitary matrices W_L and W_R such that both $W_L^\dagger Y_{\ell i} W_R$ $(i = 1, 2)$ get simultaneously diagonalized. It is well-known that the structure of the quark sector can be enforced through a $\mathbb{Z}_2$ symmetry, but this is not the case in the lepton sector. Nevertheless, as it is shown in Appendix A, the entire Yukawa structure is stable under one loop renormalization group evolution (RGE) and, therefore, the model is free from unwanted SFCNC.

Going to the fermion mass bases for our I-gℓFC model – type I in the quark sector and general flavor conserving in the lepton sector – we get the relevant new Yukawa structures:

$$\begin{aligned} \mathscr{L}_\mathrm{Y} = & -\frac{\sqrt{2}}{v} \bar{Q}_L \left(H_1 \mathrm{M}_d + H_2 \mathrm{N}_d\right) d_R \\ & -\frac{\sqrt{2}}{v} \bar{Q}_L \left(\tilde{H}_1 \mathrm{M}_u + \tilde{H}_2 \mathrm{N}_u\right) u_R \\ & -\frac{\sqrt{2}}{v} \bar{L}_L \left(H_1 \mathrm{M}_\ell + H_2 \mathrm{N}_\ell\right) \ell_R + \mathrm{H.c.}\,, \end{aligned} \tag{18}$$

with

$$\mathrm{N}_d = t_\beta^{-1} \mathrm{M}_d, \mathrm{N}_u = t_\beta^{-1} \mathrm{M}_u, \mathrm{N}_\ell = \mathrm{diag}(n_e, n_\mu, n_\tau)\,, \tag{19}$$

and M_f $(f = u, d, \ell)$ the corresponding diagonal fermion mass matrices. Note that the quark couplings N_u and N_d are those from 2HDMs of type I or X. On the other hand, the matrices N_ℓ correspond to a general flavor conserving lepton sector. Therefore, they are diagonal, arbitrary and one loop stable under RGE, as it was shown in [43], meaning that they remain diagonal.

We must stress that it is the fact that n_e and n_μ are completely independent what implements the desired decoupling between electron and muon NP couplings in order to have enough freedom to address the corresponding $(g-2)_\ell$ anomalies. We assume that these couplings are real, i.e., $\mathrm{Im}(n_\ell) = 0$. This prevents us from dangerous contributions to electric dipole moments (EDMs), that are tightly constrained: $|d_e| < 1.1 \times 10^{-29}$ e $\cdot$ cm [101].

Furthermore, we consider an scalar potential shaped by a $\mathbb{Z}_2$ symmetry that is softly broken by the term $\mu_{12}^2 \neq 0$. Hence, we have to take $\lambda_6 = \lambda_7 = 0$ in Eq. (4). We also assume that there is no CP violation in the scalar sector, so Eq. (13) is fulfilled.

Under these assumptions, the flavor conserving Yukawa interactions of neutral scalars read

$$\begin{aligned}\mathscr{L}_{\rm N} = &-\frac{m_{u_j}}{v}\left(s_{\alpha\beta}+c_{\alpha\beta}t_\beta^{-1}\right)\mathrm{h}\,\bar{u}_j u_j\\ &-\frac{m_{d_j}}{v}\left(s_{\alpha\beta}+c_{\alpha\beta}t_\beta^{-1}\right)\mathrm{h}\,\bar{d}_j d_j\\ &-\frac{m_{\ell_j}}{v}\left(s_{\alpha\beta}+c_{\alpha\beta}\frac{\mathrm{Re}\left(n_{\ell_j}\right)}{m_{\ell_j}}\right)\mathrm{h}\,\bar{\ell}_j\ell_j\\ &-\frac{m_{u_j}}{v}\left(-c_{\alpha\beta}+s_{\alpha\beta}t_\beta^{-1}\right)\mathrm{H}\,\bar{u}_j u_j\\ &-\frac{m_{d_j}}{v}\left(-c_{\alpha\beta}+s_{\alpha\beta}t_\beta^{-1}\right)\mathrm{H}\,\bar{d}_j d_j\\ &-\frac{m_{\ell_j}}{v}\left(-c_{\alpha\beta}+s_{\alpha\beta}\frac{\mathrm{Re}\left(n_{\ell_j}\right)}{m_{\ell_j}}\right)\mathrm{H}\,\bar{\ell}_j\ell_j\\ &+i\frac{m_{u_j}}{v}t_\beta^{-1}\mathrm{A}\,\bar{u}_j\gamma_5 u_j - i\frac{m_{d_j}}{v}t_\beta^{-1}\mathrm{A}\,\bar{d}_j\gamma_5 d_j\\ &-i\frac{\mathrm{Re}\left(n_{\ell_j}\right)}{v}\mathrm{A}\,\bar{\ell}_j\gamma_5\ell_j\,,\end{aligned} \tag{20}$$

and those involving charged scalars are

$$\begin{aligned}\mathscr{L}_{\rm Ch} = &\frac{\mathrm{H}^-}{\sqrt{2}v}\bar{d}_i\,V_{ji}^*t_\beta^{-1}\left[(m_{u_j}-m_{d_i})+(m_{u_j}+m_{d_i})\gamma_5\right]u_j\\ &+\frac{\mathrm{H}^+}{\sqrt{2}v}\bar{u}_j\,V_{ji}t_\beta^{-1}\left[(m_{u_j}-m_{d_i})-(m_{u_j}+m_{d_i})\gamma_5\right]d_i\\ &-\frac{\mathrm{H}^-}{\sqrt{2}v}\bar{\ell}_j\,\mathrm{Re}\left(n_{\ell_j}\right)(1-\gamma_5)\,\nu_j\\ &-\frac{\mathrm{H}^+}{\sqrt{2}v}\bar{\nu}_j\,\mathrm{Re}\left(n_{\ell_j}\right)(1+\gamma_5)\,\ell_j\,,\end{aligned} \tag{21}$$

with $i, j = 1, 2, 3$ summing over generations. It is easy to check that h presents the same couplings as the SM Higgs boson when we take the scalar alignment limit, i.e., $s_{\alpha\beta}\to 1$.

3 General constraints

Before addressing the different contributions to the anomalous magnetic moments δa_ℓ, we discuss in this section some general constraints which are relevant in the scenario under consideration. By "general" we mean that they do not depend specifically on the values of $\mathrm{Re}\,(n_e)$, $\mathrm{Re}\,(n_\mu)$, δa_e and δa_μ. Furthermore, their effects can be understood in simple terms.

- Alignment. The couplings of the scalar h, assumed to be the SM-Higgs-like particle with $m_{\rm h} = 125$ GeV, deviate from SM values through the scalar mixing in Eq. (13). Measurements of the signal strengths in the usual set of production mechanisms and decay channels impose $c_{\alpha\beta} \ll 1$. Concerning the scalar sector, we are thus in the *alignment limit*.
- Oblique parameters and M_W. Electroweak precision measurements constrain deviations in the oblique parameters S and T [97,102]:

$$\begin{aligned}&\Delta S = 0.00 \pm 0.07, \quad \Delta T = 0.05 \pm 0.06,\\ &\rho = 0.92 \text{ (correlation)}.\end{aligned} \tag{22}$$

In 2HDMs, in the alignment limit mentioned above, one can observe that the corrections to S and T are kept under control when either $m_{\rm H^\pm} \simeq m_{\rm A}$ or $m_{\rm H^\pm} \simeq m_{\rm H}$, as shown in Fig. 1a. Recently, the CDF collaboration announced a measurement of the W boson mass which disagrees with SM expectations [96]. In fits of electroweak precision observables this disagreement can be translated into values of the oblique parameters $(\Delta S, \Delta T) \neq (0, 0)$ [103,104] (although fits including ΔU have also been considered, we focus on the case $\Delta U = 0$, appropriate here). In order to "explain" the CDF M_W "anomaly" one

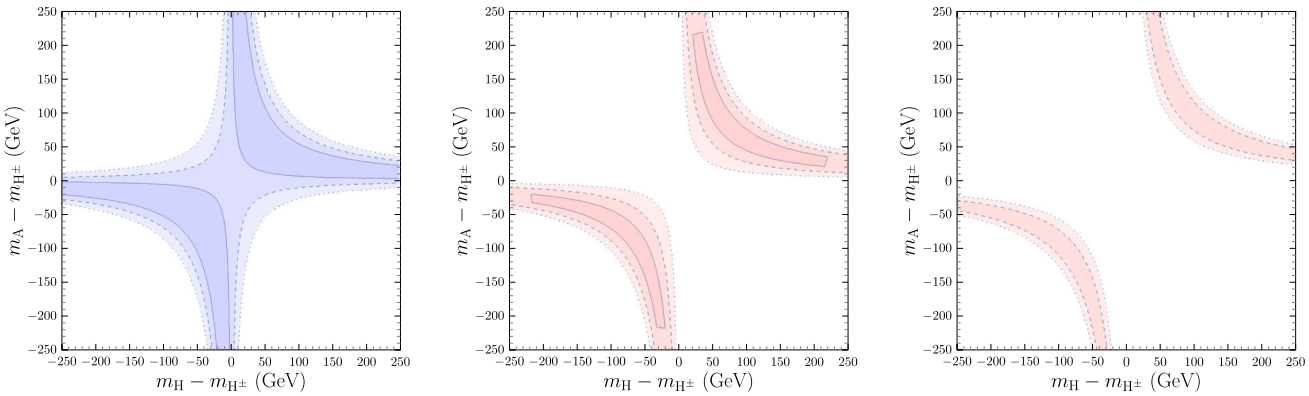

(a) $(\Delta S, \Delta T)$ in eq. (22). **(b)** $(\Delta S, \Delta T)$ in eq. (23). **(c)** $(\Delta S, \Delta T)$ in eq. (24).

Fig. 1 Oblique parameters: allowed regions in $m_{\rm A} - m_{\rm H^\pm}$ vs. $m_{\rm H} - m_{\rm H^\pm}$. Darker to lighter colors correspond to 2D-$\Delta\chi^2$ 1, 2 and 3σ regions. The plot corresponds to $m_{\rm H^\pm} = 1$ TeV and scalar alignment

can thus consider $(\Delta S, \Delta T)$ constraints from [103,104] instead of Eq. (22). We can consider, in particular,

(i) the "conservative scenario" in [103] which combines the CDF with previous measurements and gives

$$\Delta S = 0.086 \pm 0.077, \quad \Delta T = 0.177 \pm 0.070, \quad \rho = 0.89, \tag{23}$$

(ii) the results in [104] which solely use the CDF measurement and give

$$\Delta S = 0.15 \pm 0.08, \quad \Delta T = 0.27 \pm 0.06, \quad \rho = 0.93. \tag{24}$$

In the alignment limit, for $m_{\mathrm{H}^\pm} = 1$ TeV, Eqs. (23) and (24) give the allowed regions represented in Fig. 1b, c respectively. In sharp contrast with Fig. 1a, notice in Fig. 1b, c how near degeneracy of the three new scalars is excluded, and how even near degeneracies $m_{\mathrm{H}^\pm} \simeq m_{\mathrm{A}}$ or $m_{\mathrm{H}^\pm} \simeq m_{\mathrm{H}}$ are quite disfavored. Furthermore, notice that the 1σ region (2D-$\Delta\chi^2 \leq 2.23$) does not appear in Fig. 1c: contrary to Eq. (23), with Eq. (24) one cannot obtain the minimum χ^2_{Min} with $m_{\mathrm{H}^\pm} = 1$ TeV.

– $\mathrm{H}^\pm$ – induced FCNC. The charged scalar $\mathrm{H}^\pm$ can contribute to $\Delta F = 1$ and $\Delta F = 2$ FCNC processes like $b \to s\gamma$ and B_q–$\bar{B}_q$ mixings (for example, through SM-like box diagrams for B_q–$\bar{B}_q$ in which $W^\pm$ are replaced with $\mathrm{H}^\pm$). The dominant contributions involve virtual top quarks as in the SM, with couplings including now t_β^{-1} factors. Keeping those contributions within experimental bounds only allows, roughly, the colored region in Fig. 2. For each value of $m_{\mathrm{H}^\pm}$ there is a lower bound on t_β. See [105–107] for further details.

– Scalar sector perturbativity. Additional constraints on scalar masses vs. t_β arise from perturbativity requirements on the quartic coefficients of the scalar potential and from perturbative unitarity of $2 \to 2$ scattering amplitudes [108–114]. With a $\mathbb{Z}_2$ symmetric potential, it is difficult to obtain masses above 1 TeV and values of t_β larger than 8. Larger values of the masses and larger values of t_β can be nevertheless obtained with the introduction of a soft symmetry breaking term $\mu_{12}^2 \neq 0$ in Eq. (4) [114,115].

– Gluon-gluon fusion production cross section. Let us consider the production cross section of H and A through the one loop gluon-gluon fusion process. In the scalar alignment limit, one can read from Eq. (20) that the same t_β^{-1} factor applies to both pure scalar H and pure pseudoscalar A couplings with the top quark in the triangle loop:

$$\sigma(pp \to S)_{\mathrm{ggF}} \propto t_\beta^{-2} |F_S(x)|^2, \quad x = 4m_t^2/m_S^2, \quad S = \mathrm{H}, \mathrm{A}. \tag{25}$$

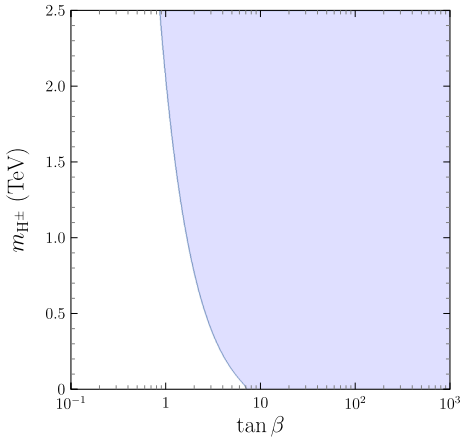

Fig. 2 $\mathrm{H}^\pm$ FCNC: $m_{\mathrm{H}^\pm}$ vs. t_β allowed region when contributions of $\mathrm{H}^\pm$ to B_q–$\bar{B}_q$ are below experimental uncertainty in ΔM_{B_q}

The corresponding loop functions F_{H} and F_{A} [116–121] are different due to the scalar or pseudoscalar character:

$$F_{\mathrm{H}}(x) = -2x(1 + (1-x)f(x)),$$
$$F_{\mathrm{A}}(x) = -2xf(x),$$
$$f(x) = \begin{cases} \arcsin^2(1/\sqrt{x}), & x \geq 1 \\ -\frac{1}{4}\left(\ln\left(\frac{1+\sqrt{1-x}}{1-\sqrt{1-x}}\right) - i\pi\right)^2, & x < 1 \end{cases}. \tag{26}$$

Figure 3 shows $|F_{\mathrm{H}}(x)|^2$, $|F_{\mathrm{A}}(x)|^2$ and the ratio $|F_{\mathrm{A}}(x)|^2/|F_{\mathrm{H}}(x)|^2$ as a function of the scalar mass. It is clear that the pseudoscalar A has a larger gluon-gluon production cross section than the scalar H for $m_{\mathrm{A}} = m_{\mathrm{H}}$ (up to a factor of 6 for $m_{\mathrm{A}} = m_{\mathrm{H}} = 2m_t$). Since dimuon searches $[pp]_{\mathrm{ggF}} \to S \to \mu^+\mu^-$ at the LHC can be rather constraining for scalar masses $m_{\mathrm{S}} < 1$ TeV, one can expect that in that low mass region $m_{\mathrm{A}} > m_{\mathrm{H}}$. One could have worried about the validity of this expectation in case $\mathrm{Br}\left(\mathrm{A} \to \mu^+\mu^-\right) \ll \mathrm{Br}\left(\mathrm{H} \to \mu^+\mu^-\right)$, but the only way to achieve a suppression of $\mathrm{Br}\left(\mathrm{A} \to \mu^+\mu^-\right)$ relative to $\mathrm{Br}\left(\mathrm{H} \to \mu^+\mu^-\right)$ is through the existence of $\mathrm{A} \to \mathrm{H}Z$ decays, which are only available if $m_{\mathrm{A}} > m_{\mathrm{H}}$, and thus cannot change that expectation.

– $e^+e^- \to \mu^+\mu^-$ at LEP. Sizable n_e and n_μ are necessary ingredients for the contributions to a_e and a_μ involving the new scalars H, A and $\mathrm{H}^\pm$. Data from LEP [122] on $e^+e^- \to \mu^+\mu^-$ with $\sqrt{s}$ up to 210 GeV are sensitive to s-channel H and A mediated contributions (contrary to the LHC gluon-gluon fusion process, being scalar or pseudoscalar does not change the sensitivity of LEP data). One can roughly expect that agreement with LEP data imposes $m_{\mathrm{A}}, m_{\mathrm{H}} \geq 210$ GeV.

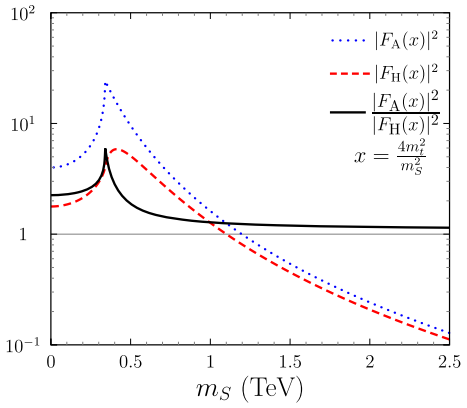

Fig. 3 Loop functions controlling gluon-gluon production cross sections of scalars

4 Contributions to δa_ℓ

The complete prediction of the anomalous magnetic moment $a_\ell^{\rm Th}$, $\ell = e, \mu$, is

$$a_\ell^{\rm Th} = a_\ell^{\rm SM} + \delta a_\ell \,, \tag{27}$$

where $a_\ell^{\rm SM}$ is the SM contribution and δa_ℓ the NP correction. The anomalies in Eqs. (1)–(3) are "solved" for $\delta a_e = \delta a_e^{\rm Exp}$ and $\delta a_\mu = \delta a_\mu^{\rm Exp}$. We introduce for convenience Δ_ℓ such that

$$\delta a_\ell = K_\ell \, \Delta_\ell, \qquad K_\ell = \frac{1}{8\pi^2}\left(\frac{m_\ell}{v}\right)^2. \tag{28}$$

For δa_μ one needs

$$\Delta_\mu \simeq 1 \,, \tag{29}$$

while for δa_e one needs

$$\Delta_e^{\rm Cs} \simeq -16 \,, \qquad \Delta_e^{\rm Rb} \simeq 9, \tag{30}$$

where the superscript corresponds to the different values in Eqs. (2) and (3).

In the model considered here, it is well known that both one loop and two loop (of Barr–Zee type) contributions can be dominant. In this section we analyse both types of contributions in the scalar alignment limit $s_{\alpha\beta} \to 1$ and keeping only leading terms in $\frac{m_\ell^2}{m_S^2}$, $S = {\rm H}, {\rm A}, {\rm H}^\pm$. Full results, used for instance in the numerical analyses, can be found in Appendix B.

4.1 One loop contributions to δa_ℓ

The one loop result $\Delta_\ell^{(1)}$ has contributions from H, A and $\rm H^\pm$. With the approximations mentioned above and the couplings in Eqs. (20) and (21), we have

$$\Delta_\ell^{(1)} \simeq |n_\ell|^2 \left(\frac{I_{\ell {\rm H}}}{m_{\rm H}^2} - \frac{I_{\ell {\rm A}} - 2/3}{m_{\rm A}^2} - \frac{1}{6 m_{{\rm H}^\pm}^2} \right), \tag{31}$$

where

$$I_{\ell S} = -\frac{7}{6} - 2\ln\left(\frac{m_\ell}{m_S}\right). \tag{32}$$

The range of interest in our analyses will be $m_S \in [0.2; 2.5]$ TeV, in which case

$$I_{\mu S} \in [13.9; 18.9], \tag{33}$$

while

$$I_{eS} = I_{\mu S} + 2\ln\left(\frac{m_\mu}{m_e}\right) = I_{\mu S} + 10.7. \tag{34}$$

In Eq. (31), the H contribution is positive, the A contribution is negative and the $\rm H^\pm$ contribution is negligible. One can then anticipate the following.

- The muon anomaly $\Delta_\mu \simeq 1$ can only be explained with the one loop H contribution and provided

$$1 \simeq \frac{|n_\mu|^2}{m_{\rm H}^2} I_{\mu {\rm H}} \;\Rightarrow\; |n_\mu| \sim \frac{1}{4} m_{\rm H}. \tag{35}$$

  Considering $|n_\mu| < 250$ GeV, a priori there could be a one loop explanation of δa_μ for $m_{\rm H} < 1$ TeV. Since the A contribution has opposite sign, if $m_{\rm A} \sim m_{\rm H}$ a substantial cancellation would occur. As discussed in Sect. 3, it is precisely for light H that one expects $m_{\rm A} > m_{\rm H}$, in which case that cancellation is largely avoided and a one loop H explanation viable. For heavier $m_{\rm H}$, the muon anomaly needs other contributions.
- For the electron Cs anomaly, $\Delta_e^{\rm Cs} \simeq -16$ can only be explained with the one loop A contribution provided

$$-16 \simeq -\frac{|n_e|^2}{m_{\rm A}^2} I_{e{\rm A}} \;\Rightarrow\; |n_e| \sim \frac{4}{5} m_{\rm A}. \tag{36}$$

  For $|n_e| < 250$ GeV, this would require the pseudoscalar A to be rather light, $m_{\rm A} < 300$ GeV. On the other hand, $m_{\rm A} > 200$ GeV would require $|n_e| > 160$ GeV: besides perturbativity concerns, such values of $|n_e|$ might be hard to reconcile with other constraints. More importantly, since we expect $m_{\rm H} < m_{\rm A}$ for light A, we also expect a sizable cancellation among H and A contributions. From this simple analysis, obtaining $\Delta_e^{\rm Cs} \simeq -16$ with one loop contributions does not appear to be feasible.
- For the electron Rb anomaly, $\Delta_e^{\rm Rb} \simeq 9$ can only be explained with the one loop H contribution and provided

$$9 \simeq \frac{|n_e|^2}{m_{\rm H}^2} I_{e{\rm H}} \;\Rightarrow\; |n_e| \sim \frac{3}{5} m_{\rm H}. \tag{37}$$

  For $m_{\rm H} > 200$ GeV, this would require $|n_e| > 120$ GeV. If the same concerns on the values of $|n_e|$ mentioned for

$\Delta_e^{\rm Cs} \simeq -16$ apply here, obtaining $\Delta_e^{\rm Rb} \simeq 9$ does not seem to be feasible neither; otherwise $\Delta_e^{\rm Rb} \simeq 9$ would be "easier" to accommodate with one loop contributions than $\Delta_e^{\rm Cs} \simeq -16$ because of the sign difference and the smaller absolute value.

4.2 Two loop contributions to δa_ℓ

The dominant two loop contributions are the Barr–Zee ones. Diagrammatically they correspond to contributions where a closed fermion loop is attached to the external lepton through two propagators: one photon and one of the new scalars H, A. In the scalar alignment limit,

$$\Delta_\ell^{(2)} = -\frac{2\alpha}{\pi}\frac{\mathrm{Re}\,(n_\ell)}{m_\ell} F. \tag{38}$$

It is important to notice that these contributions are linear in n_ℓ. Detailed expressions are provided in Appendix B. In Eq. (38) we have

$$\frac{2\alpha}{\pi m_e} \simeq 9.1\,\mathrm{GeV}^{-1}, \qquad \frac{2\alpha}{\pi m_\mu} \simeq 0.044\,\mathrm{GeV}^{-1}. \tag{39}$$

The function F depends on the masses of the fermions in the closed loop, their couplings to H and A, and on $m_{\rm A}$ and $m_{\rm H}$. Considering the dominant contributions from top and bottom quarks, and also from tau and muon leptons since n_τ and n_μ are free parameters,

$$F = \frac{t_\beta^{-1}}{3}[4(f_{t\rm H} + g_{t\rm A}) + (f_{b\rm H} - g_{b\rm A})] + \frac{\mathrm{Re}\,(n_\tau)}{m_\tau}(f_{\tau\rm H} - g_{\tau\rm A}) + \frac{\mathrm{Re}\,(n_\mu)}{m_\mu}(f_{\mu\rm H} - g_{\mu\rm A}), \tag{40}$$

with

$$f_{xS} = f\left(\frac{m_x^2}{m_S^2}\right), \quad g_{xS} = g\left(\frac{m_x^2}{m_S^2}\right). \tag{41}$$

The functions $f(z)$ and $g(z)$ are defined in Appendix B. It is to be noticed that (i) $f(z) \sim g(z)$ in the range of interest, (ii) larger values correspond to heavier fermions, (iii) for the top quark loop, f and g vary between 0.08 and 1 in the relevant range of scalar masses, $m_S \in [0.2; 2.5]$ TeV.

- If the electron anomaly is to be obtained through the two loop contributions,

$$\Delta_e \simeq -9.1\, F\, \mathrm{Re}\,(n_e)\,/\mathrm{GeV}, \tag{42}$$

and thus

$$\begin{aligned} &\text{from } \Delta_e^{\rm Cs}, \quad \mathrm{Re}\,(n_e)\ F \simeq 1.8\,\mathrm{GeV}, \\ &\text{from } \Delta_e^{\rm Rb}, \quad \mathrm{Re}\,(n_e)\ F \simeq -1.0\,\mathrm{GeV}. \end{aligned} \tag{43}$$

The sign and the magnitude of F is fixed by the $\mathrm{Re}\,(n_e)$ value to fix δa_e.

- For $m_{\rm H} > 1$ TeV, two loop contributions are necessary to explain the muon anomaly, in which case

$$\begin{aligned} \Delta_\mu &\simeq -0.044\, F\, \mathrm{Re}\left(n_\mu\right)/\mathrm{GeV} \ \Rightarrow\ \mathrm{Re}\left(n_\mu\right) \\ F &\simeq -23\,\mathrm{GeV}. \end{aligned} \tag{44}$$

If follows that, for $m_{\rm H} > 1$ TeV,

$$\begin{aligned} &\text{for } \Delta_e^{\rm Cs} \text{ and } \Delta_\mu, \quad \mathrm{Re}\left(n_\mu\right) \sim -13\mathrm{Re}\,(n_e)\,, \\ &\text{for } \Delta_e^{\rm Rb} \text{ and } \Delta_\mu, \quad \mathrm{Re}\left(n_\mu\right) \sim 23\mathrm{Re}\,(n_e)\,. \end{aligned} \tag{45}$$

These correlations show that, in the present framework, the independence of n_e and n_μ is essential to explain the different sign of $\Delta_e^{\rm Cs}$ and Δ_μ. This sign difference is challenging for many scenarios addressing simultaneously both anomalies. In this sense, addressing $\Delta_e^{\rm Rb}$ and Δ_μ is less challenging.

5 Analysis

In Sect. 3 we have discussed some general constraints that apply without regard to the values of n_e and n_μ of interest to reproduce the δa_ℓ anomalies; in Sect. 4 we have explored the obtention of the δa_ℓ anomalies through one and two loop contributions. It is now time to present the main aspects of our detailed numerical analyses. The goal of the numerical analyses is to explore the parameter space of the model and map the different regions where a chosen set of relevant constraints is satisfied and the δa_ℓ anomalies are explained in terms of the new contributions. The independent parameters of the model are $\{t_\beta, m_{\rm H}, m_{\rm A}, m_{\rm H^\pm}, \mu_{12}^2, c_{\alpha\beta}, \mathrm{Re}\,(n_e), \mathrm{Re}\left(n_\mu\right), \mathrm{Re}\,(n_\tau)\}$:$\{t_\beta, m_{\rm H}, m_{\rm A}, m_{\rm H^\pm}, \mu_{12}^2, c_{\alpha\beta}\}$ control the scalar sector (together with v and $m_{\rm h}$) while $\{\mathrm{Re}\,(n_e)\,, \mathrm{Re}\left(n_\mu\right), \mathrm{Re}\,(n_\tau)\}$ give the lepton Yukawa couplings (quark Yukawa couplings are fixed by t_β). The set of relevant constraints includes the following.

- Boundedness from below of the scalar potential [123], perturbativity of quartic couplings and perturbative unitarity of high energy $2 \to 2$ scattering in the scalar sector [110].
- Corrections to the oblique parameters S and T in agreement with electroweak precision data [97,102].
- "Production × decay" predictions for h in agreement with Higgs signal strengths [124–136]. As already mentioned, this constraint forces the alignment limit in the scalar sector: in the analyses of Sect. 6 one obtains indeed $c_{\alpha\beta} < 3 \times 10^{-3}$.
- Lepton flavor universality in leptonic and semileptonic decays [97,137,138].

– $b \to s\gamma$ and B_q^0–$\bar{B}_q^0$ data [97,105,106].
– $e^+e^- \to \mu^+\mu^-, \tau^+\tau^-$ data from LEP (with center of mass energies up to 210 GeV) [122].
– LHC searches: resonant $pp \to S \to \mu^+\mu^-, \tau^+\tau^-$ searches with gluon-gluon fusion $pp \to S$ production [139–143] and $H^\pm$ searches in $pp \to H^\pm tb$, $H^\pm \to \tau\nu, tb$ [144–147].

For additional details on the different constraints we refer to [41]. The constraints are typically modelled with a gaussian likelihood or an equivalent χ^2 term, the overall likelihood is sampled over parameter space using Markov chain Monte Carlo techniques in order to obtain the regions where (best) agreement with the constraints is obtained. There are two final aspects of central importance which require a specific discussion: (i) how are the anomalies included in the analyses, (ii) what ranges are considered for the n_ℓ parameters.
Concerning the a_ℓ anomalies, the situation for $\delta a_\mu^{\rm Exp}$ is clear: one should consider Eq. (1). On the contrary, for $\delta a_e^{\rm Exp}$ the situation is not settled: we have Eqs. (2) and (3), which are rather incompatible. In order to have a complete picture, we analyse both cases separately. Furthermore, we also consider two additional possibilities concerning $\delta a_e^{\rm Exp}$:

– despite the marginal compatibility of $\delta a_e^{\rm Exp,Cs}$ and $\delta a_e^{\rm Exp,Rb}$, we combine them into

$$\delta a_e^{\rm Exp,Avg} = -(2.0 \pm 2.2) \times 10^{-13}, \tag{46}$$

which has the same sign as $\delta a_e^{\rm Exp,Cs}$, i.e. opposite to $\delta a_\mu^{\rm Exp}$, but a size close to 4 times smaller;
– a conservative approach in which we only assume that $|\delta a_e| \leq 20\times10^{-13}$. Rather than targeting a specific value, this analysis may help to single out regions of parameter space where one cannot reproduce $\delta a_\mu^{\rm Exp}$ together with any value of δa_e compatible with $\delta a_e^{\rm Exp,Cs}$ or $\delta a_e^{\rm Exp,Rb}$.

We will refer to these separate analyses as "$a_e^{\rm Cs}$", "$a_e^{\rm Rb}$", "$a_e^{\rm Avg}$", "$a_e^{\rm Bound}$". For their implementation in the analyses, we assign a joint χ^2 contribution (corresponding to a gaussian factor in the likelihood)

$$\chi^2_{g-2}(\delta a_e, \delta a_\mu) = \left(\frac{\delta a_e - c_e}{s_e}\right)^2 + \left(\frac{\delta a_\mu - c_\mu}{s_\mu}\right)^2, \tag{47}$$

where c_ℓ is the experimental central value and s_ℓ is the experimental uncertainty *divided by 4*. The scope of this choice – dividing the experimental uncertainty by 4 instead of simply using the experimental uncertainty – is to show clearly that the model can reproduce easily and simultaneously both the muon and the electron anomalies, and to guarantee that we are definitely reproducing a sizable deviation from the SM both in a_μ and in all cases for a_e, except the "$a_e^{\rm Bound}$" analysis where there is no δa_e term in Eq. (47) and $|\delta a_e| \leq 20\times10^{-13}$ is imposed. As a summary, all four selected cases of $\delta a_\mu^{\rm Exp}$ vs. $\delta a_e^{\rm Exp}$ are represented in Fig. 4.

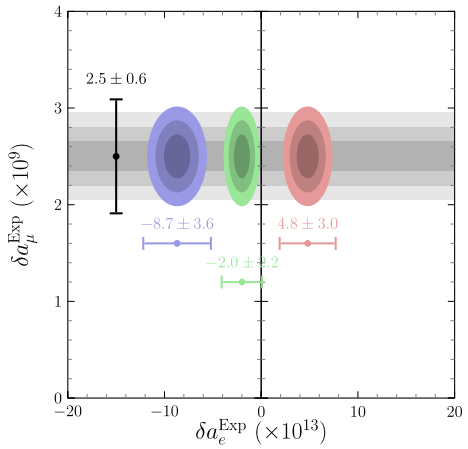

Fig. 4 Allowed $\delta a_\mu^{\rm Exp}$ vs. $\delta a_e^{\rm Exp}$ regions in the different analyses

The different colored regions in Fig. 4 represent three contours in the joint $\Delta\chi^2 = \chi^2 - \chi^2_{\rm Min}$ considering only Eq. (47). In a 2D-$\Delta\chi^2$ distribution they correspond, darker to lighter, to 1, 2 and 3σ regions with 68.2% C.L., 95.4% C.L. and 99.7% C.L., respectively. The same color coding is used in the figures below illustrating the final results of the analyses, where all observables and constraints have been included.
Finally, in [41], only $|n_\ell| \leq 100$ GeV were considered. Although for $|n_e|, |n_\mu| \sim 100$ GeV lepton couplings to the new scalars are hugely enhanced with respect to h couplings, it is true that $\frac{|n_\ell|}{v} \sim \frac{100\,\text{GeV}}{v} \sim 0.4$ does not appear to pose a perturbativity challenge. In fact, the one loop correction to the imaginary part of the $m_{\rm H}$ mass is controlled by $\Gamma(H \to \ell\bar{\ell})$ and the relevant ratio is $\frac{\Gamma}{m_{\rm H}} = \frac{1}{8\pi}\frac{|n_\ell|^2}{v^2}$, therefore arriving to $|n_\ell| = v \sim 250$ GeV represents one loop corrections at the 4% level. For this reason the analyses have been done with $|n_\ell| \leq 250$ GeV $\sim v$; furthermore, the analysis "$a_e^{\rm Cs}$" has been conducted both with $|n_\ell| \leq 100$ GeV (since this case is the closest one to [41]) and with $|n_\ell| \leq 250$ GeV.

6 Results

In the next subsections we discuss the most relevant results of the analyses done following the lines of the previous section. In Sect. 6.1 we consider the scenario "$a_e^{\rm Cs}$" when $|n_\ell| \leq 100$ GeV is imposed. The implications of changing this last assumption to $|n_\ell| \leq 250$ GeV are addressed in Sect. 6.2. The implications of the different assumptions for the electron anomaly, that is scenarios "$a_e^{\rm Rb}$", "$a_e^{\rm Avg}$" and "$a_e^{\rm Bound}$" are explored in Sect. 6.3. The impact of the recent measurement of M_W by the CDF collaboration is considered in Sect. 6.4.

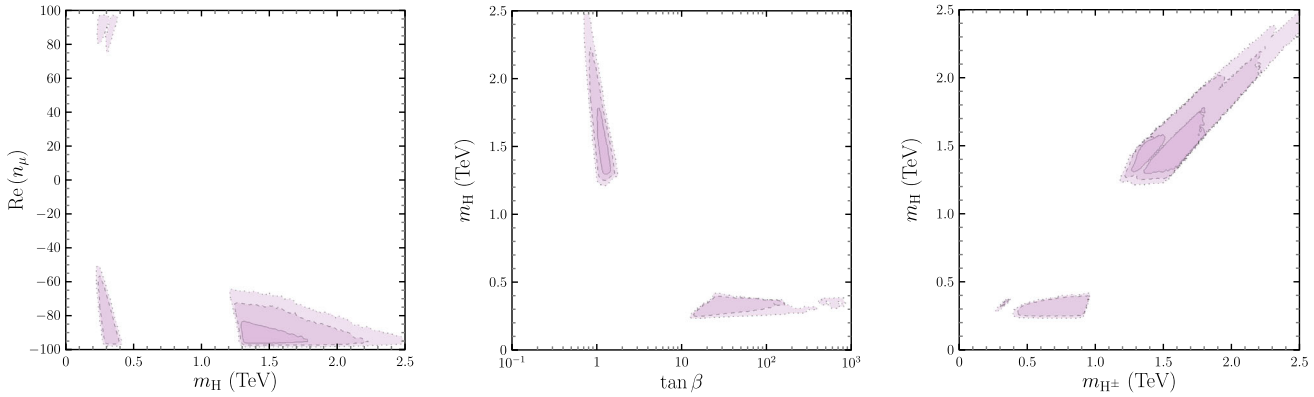

(a) Re $\left(n_\mu\right)$ vs. $m_{\rm H}$. **(b)** $m_{\rm H}$ vs. t_β. **(c)** $m_{\rm H}$ vs. $m_{\rm H^\pm}$.

Fig. 5 Allowed regions: relevant correlations involving $m_{\rm H}$ with $|n_\ell| \leq 100$ GeV

Finally, to further illustrate these discussions, a few complete example cases are shown in Sect. 6.5.

6.1 $|n_\ell| \leq 100$ GeV

Here we present the results of the analysis "$a_e^{\rm Cs}$" with the perturbativity constraint $|n_\ell| \leq 100$ GeV. This serves to revisit the main results of [41] and as a reference for the analysis with $|n_\ell| \leq 250$ GeV addressed in the following subsection.

The perturbativity constraint limits the possibility of explaining $\delta a_e^{\rm Exp,Cs}$ via the one loop contribution, since it requires $m_{\rm A} \leq 125$ GeV for $|n_e| \leq 100$ GeV (see Eq. (36)) which is not allowed by $e^+e^- \to \mu^+\mu^-$ LEP data. On that respect, lepton flavor universality constraints also limit the possibility of a one loop explanation for the electron anomaly, as discussed later. This leaves us with two scenarios, one where both anomalies are explained via the two loop contribution, following the scaling law in Eq. (45), and another where the muon anomaly is one loop dominated while the electron one is still generated at two loops.

In Fig. 5a the allowed regions for Re $\left(n_\mu\right)$ are presented as a function of $m_{\rm H}$. Three disjoint regions in the scalar mass can be seen: two in the 200–400 GeV range and the other above 1.2 TeV. The low mass regions belong to the scenario where the muon anomaly is obtained through the one loop contribution in agreement with the relation in Eq. (35). Note that this contribution depends on the absolute value of the coupling, so both signs are allowed for Re $\left(n_\mu\right)$. In the large mass region both leptonic anomalies are two loop dominated. Figure 5b shows $m_{\rm H}$ vs. t_β. It contains two separate allowed regions again: in the $t_\beta \sim 1$ regime only scalar masses above 1.2 TeV are allowed; conversely for t_β larger than 10, $m_{\rm H}$ lies in the 200–400 GeV interval.

To complement the previous two plots, in Fig. 5c the relation between the masses $m_{\rm H}$ and $m_{\rm H^\pm}$ is shown. In the low mass region we can clearly distinguish two scenarios. One where $m_{\rm H^\pm} \simeq m_{\rm H}$ and another where $m_{\rm H^\pm} > m_{\rm H}$; in the latter, $m_{\rm H^\pm} \simeq m_{\rm A}$.The degeneracy of $\rm H^\pm$ with either H or A arises from the oblique parameters constraint, as mentioned in Sect. 3. In the large mass region the mass differences do not exceed ± 300 GeV.

Figure 6 illustrates the allowed regions for the resonant process $[pp]_{\rm ggF} \to S \to \mu^+\mu^-$ with respect to the scalar mass m_S for $S = {\rm H}, {\rm A}$. The black line corresponds to the limit observed by CMS [140]. Although LHC direct searches are already constraining the allowed regions, there is ample room for extra scalars that can explain both $g-2$ anomalies simultaneously.

Let us now discuss some results concerning Re (n_e) and Re (n_τ). With a two loop explanation of the electron anomaly, it follows from Eqs. (38) and (40) (see Appendix B for further details) that one could have expected that both the coupling Re (n_e) and the deviation δa_e have opposite sign: this is confirmed in Fig. 7 in the 1σ region. However, this figure also contains regions where Re (n_e) is negative. This behavior might be understood by analysing with some detail the two loop contribution to δa_e: F in Eq. (40) can be decomposed as $F = F_q + F_\tau + F_\mu$, where F_f is the contribution with fermion f running in the closed loop. One can estimate the importance of the different contributions for different t_β, $m_{\rm H}$ and $m_{\rm A}$ ranges.

– For $t_\beta \sim 1$ and $m_{\rm H}, m_{\rm A} > 1.2$ TeV, Eq. (40) gives

$$F_q > 0.18, \quad |F_\tau| < 0.13 \times 10^{-4} \frac{\text{Re}\,(n_\tau)}{1\ \text{GeV}}, \quad \left|F_\mu\right| < 0.12 \times 10^{-5} \frac{\text{Re}\left(n_\mu\right)}{1\ \text{GeV}}. \tag{48}$$

It is clear that in this region the quark-induced contribution F_t is (i) necessarily dominant and (ii) it requires

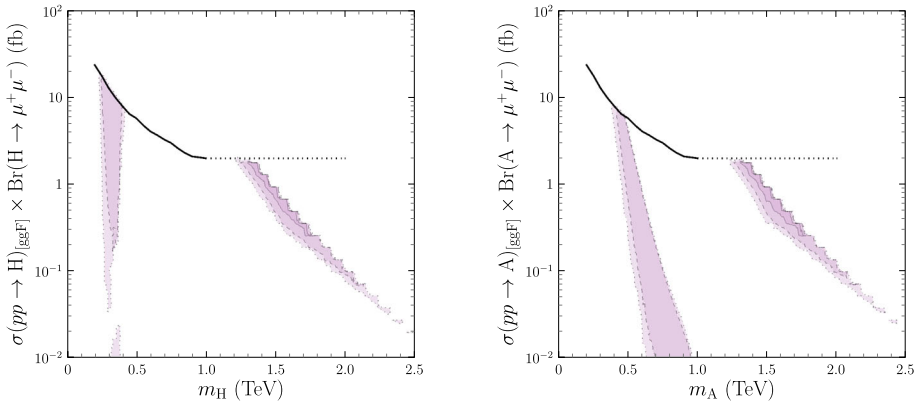

(a) For $S = \mathrm{H}$. **(b)** For $S = \mathrm{A}$.

Fig. 6 $\sigma(pp \to S)_{[\mathrm{ggF}]} \times \mathrm{Br}\left(S \to \mu^+\mu^-\right)$ vs. m_S allowed regions with $|n_\ell| \leq 100$ GeV

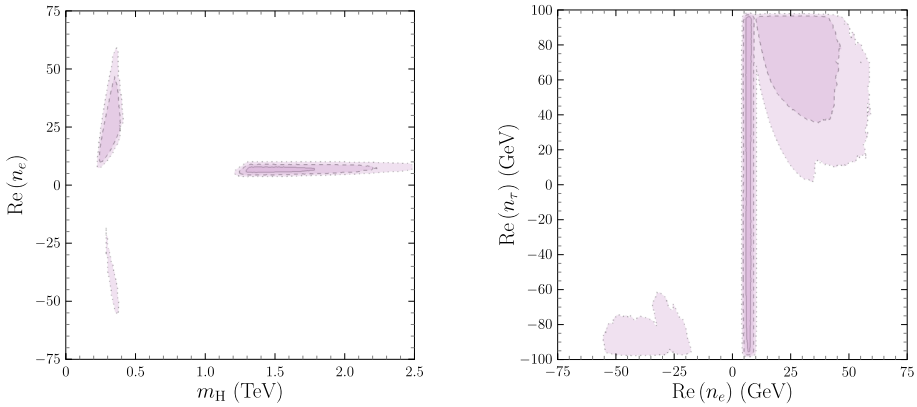

(a) $\mathrm{Re}\,(n_e)$ vs. m_{H}. **(b)** $\mathrm{Re}\,(n_\tau)$ vs. $\mathrm{Re}\,(n_e)$.

Fig. 7 Allowed regions for $\mathrm{Re}\,(n_e)$ with $|n_\ell| \leq 100$ GeV

$\mathrm{Re}\,(n_e) \sim 4{-}10$ GeV, as Fig. 7a illustrates, in order to reproduce $\Delta_e^{\mathrm{Cs}} \simeq -16$.

– For $t_\beta > 10$, $m_{\mathrm{H}} \in [200, 400]$ GeV and $m_{\mathrm{A}} \in [400, 1000]$ GeV, Eq. (40) gives

$$F_q < 0.18, \quad F_\tau \in [0.02, 0.15] \times 10^{-2} \frac{\mathrm{Re}\,(n_\tau)}{1\ \mathrm{GeV}}, \\ F_\mu \in [0.04, 0.25] \times 10^{-3} \frac{\mathrm{Re}\,(n_\mu)}{1\ \mathrm{GeV}}. \tag{49}$$

In this case, large values of $\mathrm{Re}\,(n_\tau) \simeq \pm 100$ GeV give τ-induced contributions at the same level of, or even larger than, the quark-induced contribution. This occurs despite some cancellation among the $\tau\mathrm{H}$ and $\tau\mathrm{A}$ contributions in Eq. (40). This scenario would require $\mathrm{Re}\,(n_e) \lesssim -15$ GeV or $\mathrm{Re}\,(n_e) \gtrsim 7$ GeV, as shown in Fig. 7a, in order to reproduce $\Delta_e^{\mathrm{Cs}} \simeq -16$.

From this simple estimates one can conclude that, besides the expected regions where δa_e arises from quark-induced two loop contributions, regions where the τ-induced contributions have an important role might be present. For this to occur, one might expect some peculiarities: besides light H and large t_β, large values of both $|\mathrm{Re}\,(n_\tau)|$ and $|\mathrm{Re}\,(n_e)|$, with $\mathrm{Re}\,(n_\tau)$ and $\mathrm{Re}\,(n_e)$ having the same sign, are required. Contrary to the case with dominating quark-induced contributions, one might then have allowed regions where $\mathrm{Re}\,(n_e) < 0$. This is illustrated in Fig. 7a, b where one can observe how allowed $\mathrm{Re}\,(n_e) < 0$ only appear for a light H, and how the regions with large $\pm\mathrm{Re}\,(n_e)$ correspond to large $\pm\mathrm{Re}\,(n_\tau)$.

To close this subsection, it is worth analysing in detail the role of the lepton flavor universality constraints mentioned in Sect. 5. As justified later, we focus on observables involving only μ's and e's. For the ratios

$$R_{\mu e}^P = \frac{\Gamma(P^+ \to \mu^+\nu)}{\Gamma(P^+ \to \mu^+\nu)_{\mathrm{SM}}} \frac{\Gamma(P^+ \to e^+\nu)_{\mathrm{SM}}}{\Gamma(P^+ \to e^+\nu)}, \tag{50}$$

the current constraints are [97]

$$R_{\mu e}^\pi = 1 + (4.1 \pm 3.3) \times 10^{-3}, \\ R_{\mu e}^K = 1 - (4.8 \pm 4.7) \times 10^{-3}. \tag{51}$$

In the present scenario,

$$R_{\mu e}^P = \frac{|1 - \Delta_\mu^P|^2}{|1 - \Delta_e^P|^2}, \quad |1 - \Delta_\ell^P|^2 = \left| 1 - \frac{M_P^2}{t_\beta m_{\mathrm{H}^\pm}^2} \frac{\mathrm{Re}\,(n_\ell)}{m_\ell} \right|^2, \tag{52}$$

and thus, for $\Delta_\ell^P \ll 1$,

$$R_{\mu e}^P \simeq 1 + 2\frac{M_P^2}{t_\beta m_{\mathrm{H}^\pm}^2}\left(\frac{\mathrm{Re}\,(n_e)}{m_e} - \frac{\mathrm{Re}\,(n_\mu)}{m_\mu}\right). \tag{53}$$

The presence of M_P^2 and the lepton masses allows us to concentrate on $R_{\mu e}^K$ and neglect the n_μ contribution. Therefore from Eq. (51) we get the constraint

$$\mathrm{Re}\,(n_e) < 5\frac{t_\beta m_{\mathrm{H}^\pm}^2}{1\ \mathrm{TeV}^2}\ \mathrm{GeV}. \tag{54}$$

Then,

- for $t_\beta \simeq 1$ and $m_{\mathrm{H}^\pm} \simeq 2$ TeV, $\mathrm{Re}\,(n_e) < 20$ GeV,
- while for $t_\beta \simeq 10^2$ and $m_{\mathrm{H}^\pm} \simeq 0.5$ TeV, $\mathrm{Re}\,(n_e) < 125$ GeV.

From muon decay constraints on the $\mathrm{H}^\pm$ mediated contributions we also have a t_β independent constraint (since the process is purely leptonic) [97,107]:

$$\left|\frac{n_e n_\mu}{m_{\mathrm{H}^\pm}^2}\right| < 0.035. \tag{55}$$

This constraint is relevant for the low mass region: for $\mathrm{Re}\,(n_\mu) \simeq 100$ GeV, we can rewrite

$$|n_e| < 87\left(\frac{m_{\mathrm{H}^\pm}}{0.5\ \mathrm{TeV}}\right)^2\ \mathrm{GeV}, \tag{56}$$

which is more restrictive than the bound from $R_{\mu e}^K$ above. Concerning other observables involving τ leptons, semileptonic processes are not sensitive to n_τ due to $\frac{m_e}{m_\tau}$ and $\frac{m_\mu}{m_\tau}$ suppressions, while purely leptonic decays have looser bounds than Eq. (55).

This simple numerical exercise confirms that $\delta a_e^{\mathrm{Exp}}$ cannot be explained through one loop contributions.

6.2 $|n_\ell| \leq 250$ GeV

As previously motivated, perturbativity bounds on the Yukawa couplings should be studied in detail. Here we explore higher scales in n_ℓ, namely changing from $|n_\ell| \leq 100$ GeV to $|n_\ell| \leq 250$ GeV while maintaining the same constraints of the previous section. Conversely to what one would naively expect, it is not just the allowed regions in the different n_ℓ that might change, but it has direct consequences on other physical observables such as the scalar masses and t_β, among others.

Figure 8a shows results for $\mathrm{Re}\,(n_\mu)$ vs. m_{H}. It is clear that the allowed regions in parameter space are notably enlarged with respect to those in Fig. 5a, which are completely embedded in the ones of this new analysis, as one could have expected. On that respect, one may realize of the appearance of a new set of intermediate values for the scalar mass, $m_{\mathrm{H}} \in [0.4; 1.2]$ TeV, when increasing our perturbativity upper bound. It can be easily understood by tracing an horizontal line at $\mathrm{Re}\,(n_\mu)_0 = -100$ GeV: we eliminate the blue region "bridge" connecting the low and high mass solutions. Therefore, this new range of scalar masses requires large values of $|\mathrm{Re}\,(n_\mu)|$.

To fully characterize the impact of perturbativity on the allowed parameter space, Fig. 8b illustrates the scalar mass m_{H} in terms of t_β. Taking into account the appearance of new intermediate solutions in m_{H}, one could expect that this behavior is translated into t_β. As Fig. 8b corroborates, new values of t_β, roughly in the range $1 \leq t_\beta \leq 10$, are allowed when changing the perturbativity requirement from $|n_\ell| \leq 100$ GeV to $|n_\ell| \leq 250$ GeV. Furthermore, one may also notice by comparing with Fig. 5b that the top blue region for large m_{H} becomes wider, around a factor 2.5 in t_β for each value of the scalar mass.

Figure 8c shows correlations among the scalar masses m_{H} and $m_{\mathrm{H}^\pm}$. Concerning the low mass regions where $\mathrm{H}^\pm$ is

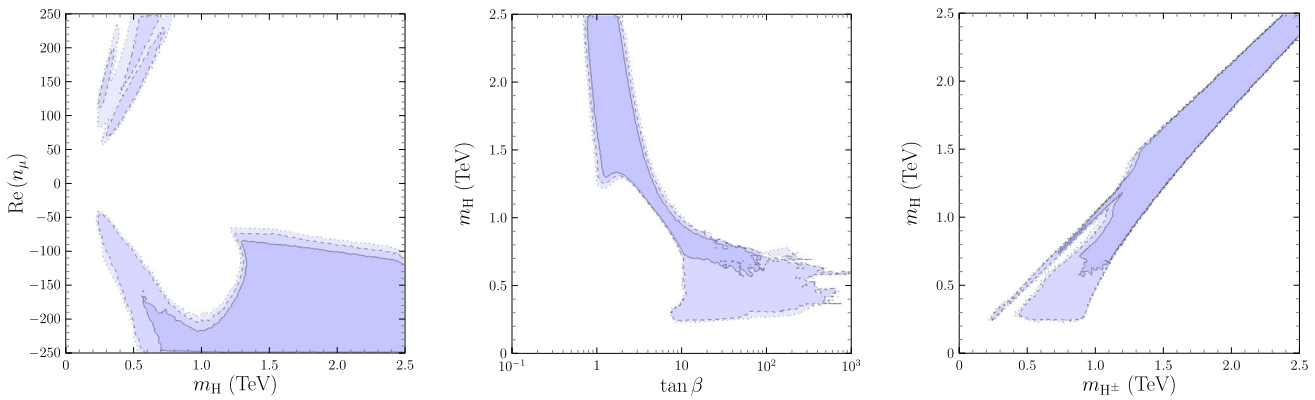

(a) $\mathrm{Re}\,(n_\mu)$ vs. m_{H}. **(b)** m_{H} vs. t_β. **(c)** m_{H} vs. $m_{\mathrm{H}^\pm}$.

Fig. 8 Allowed regions: relevant correlations involving m_{H} with $|n_\ell| \leq 250$ GeV

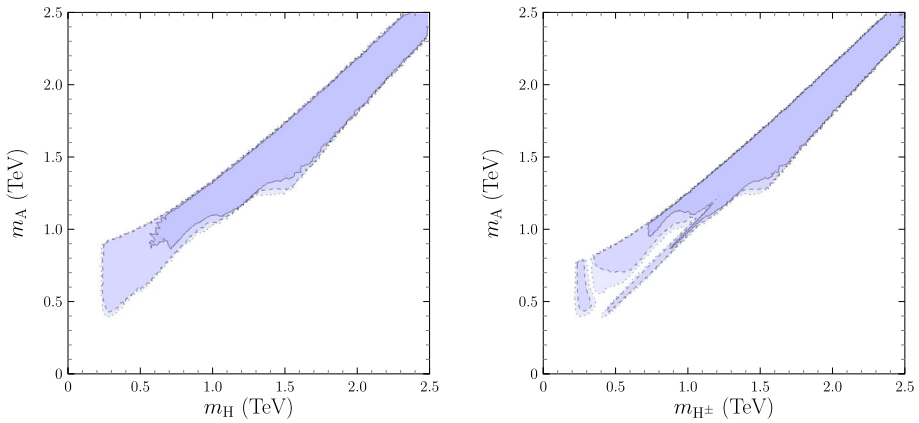

Fig. 9 Allowed regions for scalar masses with $|n_\ell| \leq 250$ GeV

(a) m_A vs. m_H. **(b)** m_A vs. $m_{H^\pm}$.

degenerate either with H or A, already mentioned in Fig. 5c, it can be observed that enlarging perturbativity bounds pushes the upper limit of these regions in such a way that $m_{H^\pm} \in [0.2; 1.2]$ TeV for $m_{H^\pm} \simeq m_H$ and $m_{H^\pm} \in [0.4; 1.2]$ TeV for $m_{H^\pm} \simeq m_A$, to a high degree of accuracy. Figure 9a, b complete the results for the scalar masses. For instance, it is still true that $m_A > m_H$ in the low mass region, according to the general constraints presented in Sect. 3.

On the other hand, Fig. 10 shows the resonant process $[pp]_{ggF} \to S \to \mu^+\mu^-$ as a function of the scalar mass m_S for $S = H, A$, which acquire an important role since we may be entering an era of exclusion or discovery at the LHC. As disclosed above, the existence of an intermediate set of solutions, $m_H \in [0.4; 1.2]$ TeV and $m_A \in [0.9; 1.2]$ TeV, opens the possibility to detect a sizeable signal in that range of scalar masses that was not contemplated in Fig. 6. Moreover, it is clear that increasing $|n_\ell|$ up to $|n_\ell| \leq 250$ GeV modifies our expectations for $\text{Br}\left(S \to \ell^+\ell^-\right)$ and, in particular, enlarges the allowed parameter space, as one can easily check.

Finally, we should stress some aspects concerning $\text{Re}\,(n_e)$ and $\text{Re}\left(n_\mu\right)$ from Fig. 11. In spite of increasing our perturbativity bound up to $|n_\ell| \leq 250$ GeV, it still seems difficult to obtain a one loop explanation for the electron anomaly since it requires quite large couplings, namely $|n_e| > 160$ GeV in the Cs case. Figure 11b shows that $|n_e| < 150$ GeV in the relevant range of scalar masses, thus indicating that $\delta a_e^{\text{Exp,Cs}}$ is mainly explained at two loops. This agrees with the discussion on universality constraints closing Sect. 6.1. As it was already explained in the discussion of Fig. 7a, now in Fig. 11b and for large scalar masses, one can easily check that the electron coupling is positive and lies in the range $\text{Re}\,(n_e) \sim 4-20$ GeV. Furthermore, according to Eq. (45), there exists a linear relation between $\text{Re}\left(n_\mu\right)$ and $\text{Re}\,(n_e)$ for $m_H > 1.2$ TeV, which implies that they have opposite sign in the Cs case and therefore $\text{Re}\left(n_\mu\right)$ should be negative in this region. The region $\text{Re}\left(n_\mu\right) = -13\text{Re}\,(n_e)$ can be seen in the lower part of Fig. 11a inside the 1σ region as it should. Departure from this straight line introduces an important one loop contribution to the muon anomaly lowering also the scalar masses ranges. On the other hand, for light scalar masses, $\text{Re}\,(n_e)$ might be either positive or negative by the same arguments discussed in Sect. 6.1. It is also important to recall that, in this low mass region, Δ_μ receives dominant one loop contributions and thus $\text{Re}\left(n_\mu\right)$ could naturally appear with both signs. From Fig. 11a, one may notice

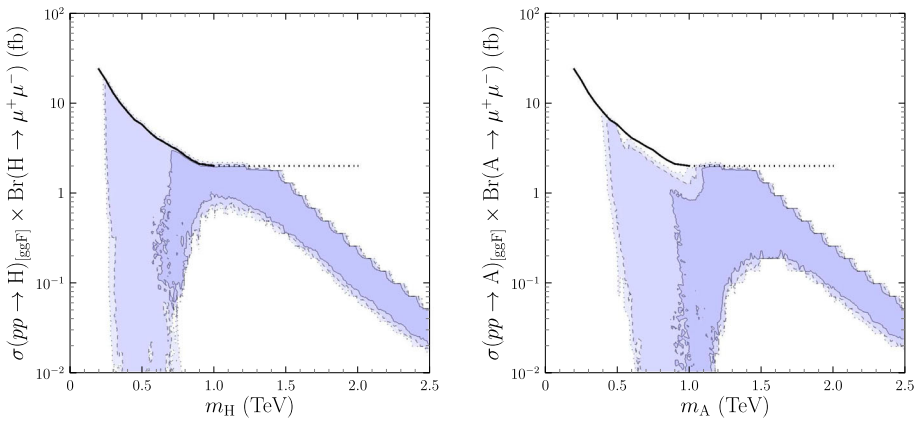

Fig. 10 $\sigma(pp \to S)_{[ggF]} \times \text{Br}\left(S \to \mu^+\mu^-\right)$ vs. m_S allowed regions with $|n_\ell| \leq 250$ GeV

(a) For $S = H$. **(b)** For $S = A$.

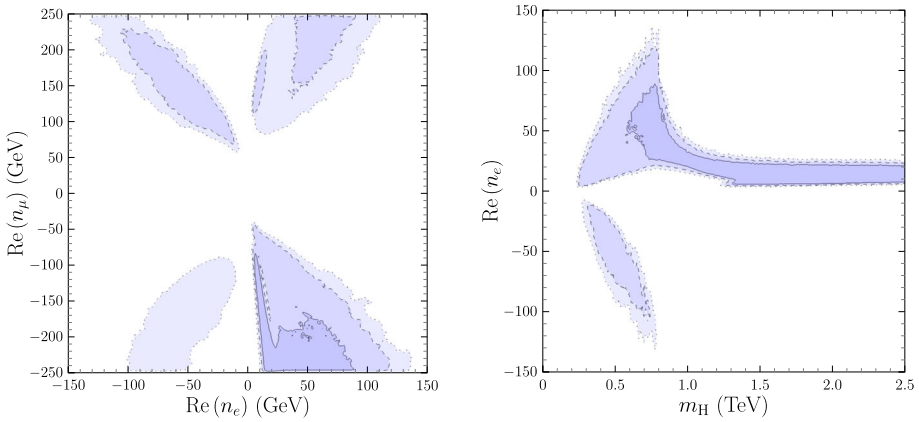

(a) Re $\left(n_\mu\right)$ vs. Re $\left(n_e\right)$. **(b)** Re $\left(n_e\right)$ vs. $m_{\rm H}$.

Fig. 11 Allowed regions for Re (n_e) with $|n_\ell| \leq 250$ GeV

as well that $|n_\mu|$ is in general larger than $|n_e|$ in the whole parameter space.

6.3 Different δa_e

As commented in Sect. 5, the situation concerning $\delta a_e^{\rm Exp}$ is to some extent unclear. In this section we discuss the implications of different assumptions for the value of $\delta a_e^{\rm Exp}$, that is, in terms of the model, the implications of requiring different values of the new contributions δa_e. The ultimate answer is definitely provided by repeating detailed numerical analyses under the different assumptions $\delta a_e^{\rm Exp}$. However, one can anticipate part of the answer with simple considerations. As analysed in Sect. 4, δa_e arises from two loop contributions proportional to Re (n_e): this fact, together with the results of Sect. 6.2 corresponding to $\delta a_e \simeq \delta a_e^{\rm Exp,Cs}$, can give us a first insight. Consider for example an allowed point in parameter space (i.e. a point respecting all imposed constraints) which gives $\delta a_e \simeq \delta a_e^{\rm Exp,Cs}$. This point has a certain Re $(n_e) =$ Re $(n_e)_{\rm Cs}$; it is straightforward that changing Re $(n_e) \mapsto$ Re $(n_e)' =$ Re $(n_e)_{\rm Rb} =$ Re $(n_e)_{\rm Cs} \times \frac{\delta a_e^{\rm Exp,Rb}}{\delta a_e^{\rm Exp,Cs}}$ and no other parameter, one would obtain $\delta a_e \simeq \delta a_e^{\rm Exp,Rb}$. The question is, of course, if such a change in Re (n_e) alone still gives an allowed point. On that respect, one needs to analyse which observables constrain Re (n_e) and how those constraints work. These are the ones related to lepton flavor universality in leptonic decays $\ell_i \to \ell_j \nu\bar{\nu}$ and in semileptonic decays involving kaons and pions, analysed in Sect. 6.1. In particular, attending to $\delta a_e^{\rm Exp,Cs}$, $\delta a_e^{\rm Exp,Rb}$ and $\delta a_e^{\rm Exp,Avg}$ in Eqs. (2), (3) and (46), one is interested in the effect on those constraints of

$$\begin{aligned} \text{Re}\,(n_e) &= \text{Re}\,(n_e)_{\rm Cs} \mapsto \text{Re}\,(n_e)' \\ &= \text{Re}\,(n_e)_{\rm Rb} = -0.55\text{Re}\,(n_e)_{\rm Cs}\,, \\ \text{Re}\,(n_e) &= \text{Re}\,(n_e)_{\rm Cs} \mapsto \text{Re}\,(n_e)' \\ &= \text{Re}\,(n_e)_{\rm Avg} = 0.23\text{Re}\,(n_e)_{\rm Cs}\,, \end{aligned} \tag{57}$$

when no other parameter is changed. There are two different aspects:

1. since $|\text{Re}\,(n_e)_{\rm Avg}|, |\text{Re}\,(n_e)_{\rm Rb}| < |\text{Re}\,(n_e)_{\rm Cs}|$, the constraint on $|n_e|$ from $\mu \to e\nu\bar{\nu}$ decays in Eq. (56) is necessarily less restrictive when Eq. (57) is considered;
2. besides the uncertainty in $R_{\mu e}^K$ in Eq. (51), as discussed previously, there is a "sign" question concerning the deviation, at the same $\simeq 5 \times 10^{-3}$ level of the uncertainty, from $R_{\mu e}^K = 1$. In order to obtain $\delta a_e \simeq \delta a_e^{\rm Exp,Cs} < 0$, the expectation is Re $(n_e) > 0$, and that produces $R_{\mu e}^K - 1 > 0$ in Eq. (53), which goes "in the wrong direction". For both cases in Eq. (57), that problem is alleviated.

It is then clear that the analysis with $\delta a_e^{\rm Exp,Cs}$ is somehow a "worst case" scenario in terms of the dependence of the constraints on Re (n_e): besides the naive mapping of allowed regions expected from Eq. (57), one might then expect larger allowed regions not only for Re (n_e) but also for other quantities of interest. As mentioned in Sect. 5, we also perform an analysis where $|\delta a_e| \leq 20 \times 10^{-13}$ is imposed (instead of requiring some specific value, as summarized in Fig. 4). This serves a double purpose: identifying which allowed regions are necessary in order to obtain an appropriate δa_μ without regard to δa_e, and identifying which regions are absolutely excluded for any value of δa_e reasonably compatible with $\delta a_e^{\rm Exp,Cs}$ or $\delta a_e^{\rm Exp,Rb}$ that one could consider.

In Figs. 12, 13 and 14, the color coding follows Fig. 4. Figure 12 shows Re $\left(n_\mu\right)$ vs. Re (n_e) and Re (n_e) vs. $m_{\rm H}$ allowed regions: comparison with Fig. 11a, b confirms the simple expectations of the previous discussion in terms of the position of the allowed regions and their extension. The same applies to Fig. 13, which shows Re $\left(n_\mu\right)$ vs. $m_{\rm H}$ (to be compared with Fig. 8a). In particular it is clear from Fig. 13c that once $\delta a_\mu \simeq \delta a_\mu^{\rm Exp}$ is imposed, the allowed regions for some parameters (besides Re $\left(n_\mu\right)$, obviously) are coarsely deter-

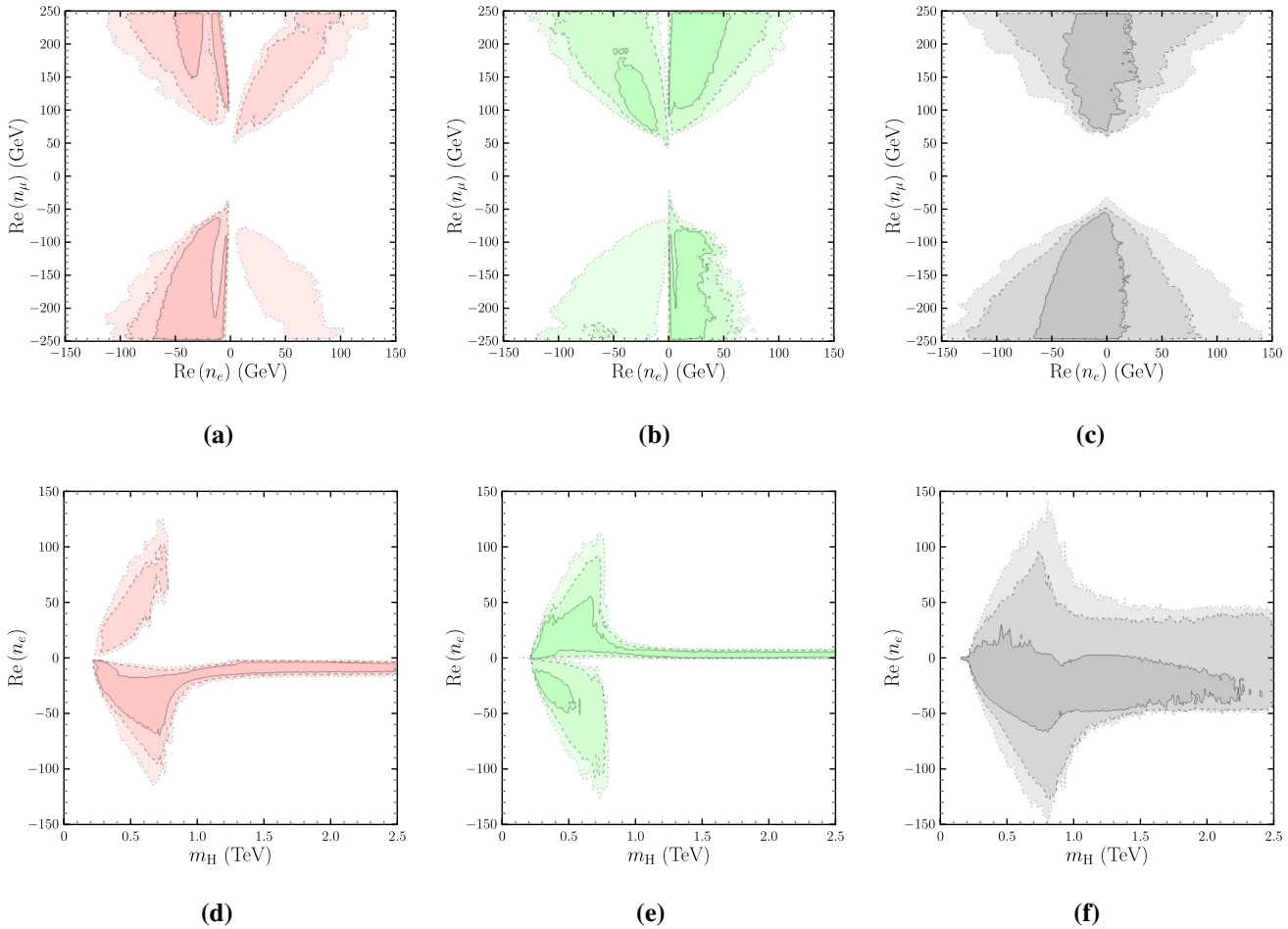

Fig. 12 Re (n_e) correlations

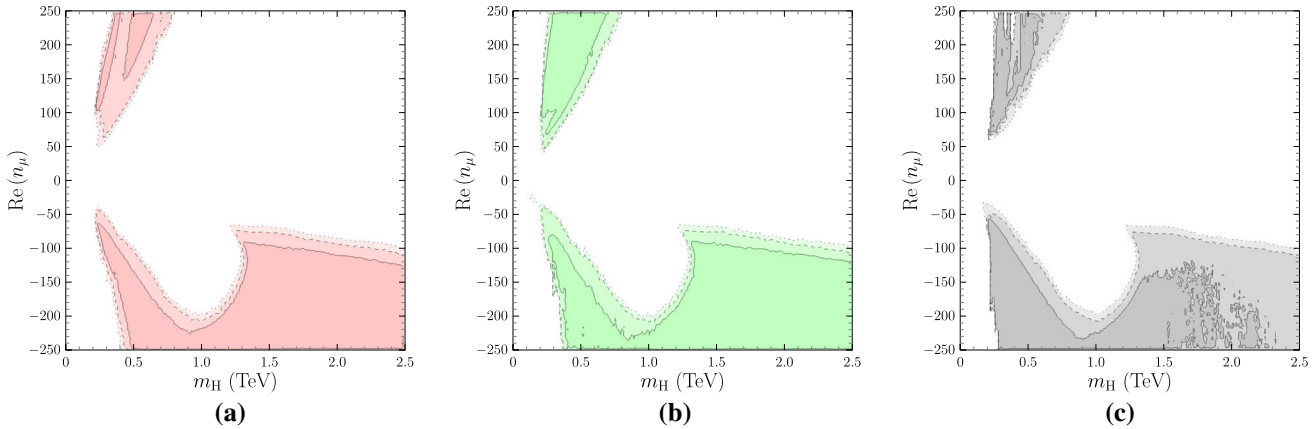

Fig. 13 Re $\left(n_\mu\right)$ vs. m_{H} correlations

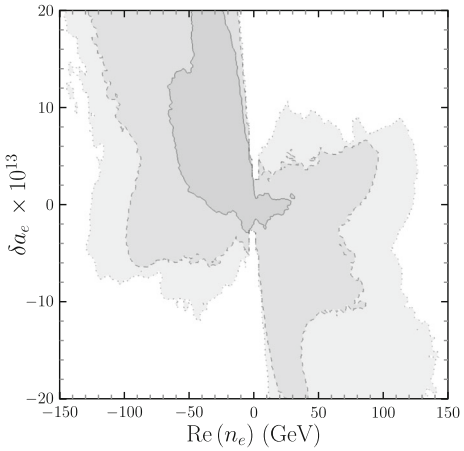

Fig. 14 δa_e vs. Re (n_e)

mined and the sensitivity of the analysis on the requirement for δa_e only concerns a finer level of detail.

There is a final point that the analysis with $|\delta a_e| \leq 20 \times 10^{-13}$ confirms. Figure 14 shows δa_e vs. Re (n_e): under the simple expectations for the two loop contributions discussed in Sect. 4.2, one would have Re $(n_e) \times \delta a_e < 0$. Besides that expected region, one can observe smaller allowed regions where Re $(n_e) \times \delta a_e > 0$: they correspond to the unexpected situation in which the two loop contributions are dominated by virtual τ's in the fermion loop, and furthermore it is clear that the values of δa_e that can be obtained in this manner are more restricted, with $|\delta a_e| < 10^{-12}$.

6.4 The CDF M_W anomaly

As mentioned in Sect. 3, one can use deviations from the SM in the oblique parameters $(\Delta S, \Delta T) \neq (0, 0)$ in order to "explain" the CDF measurement of M_W in [96]: this subsection is devoted to that "explanation". Figures 15 and 16 show results analogous to the ones in Sect. 6.2 – which use Eq. (22) – except for a different $(\Delta S, \Delta T)$ constraint. Figure 15 is obtained with Eq. (23) (the "conservative" average of [103]) and Fig. 16 is obtained with Eq. (24) (the results in [104]). The coloring of the allowed regions corresponds, darker to lighter, to 1, 2, 3σ levels of a 2D-$\Delta\chi^2$. For $\Delta\chi^2$ we use the χ^2_{Min} value of the analysis in Sect. 6.2 (that is, with the constraint in Eq. (22) for ΔS, ΔT). A few comments are in order.

– Besides the absence of degeneracies $m_{\text{H}^\pm} \simeq m_{\text{H}}$ or $m_{\text{H}^\pm} \simeq m_{\text{A}}$, masses of the new scalars larger than 2 TeV are more difficult to accommodate. This can be understood attending to the clash between the mass differences

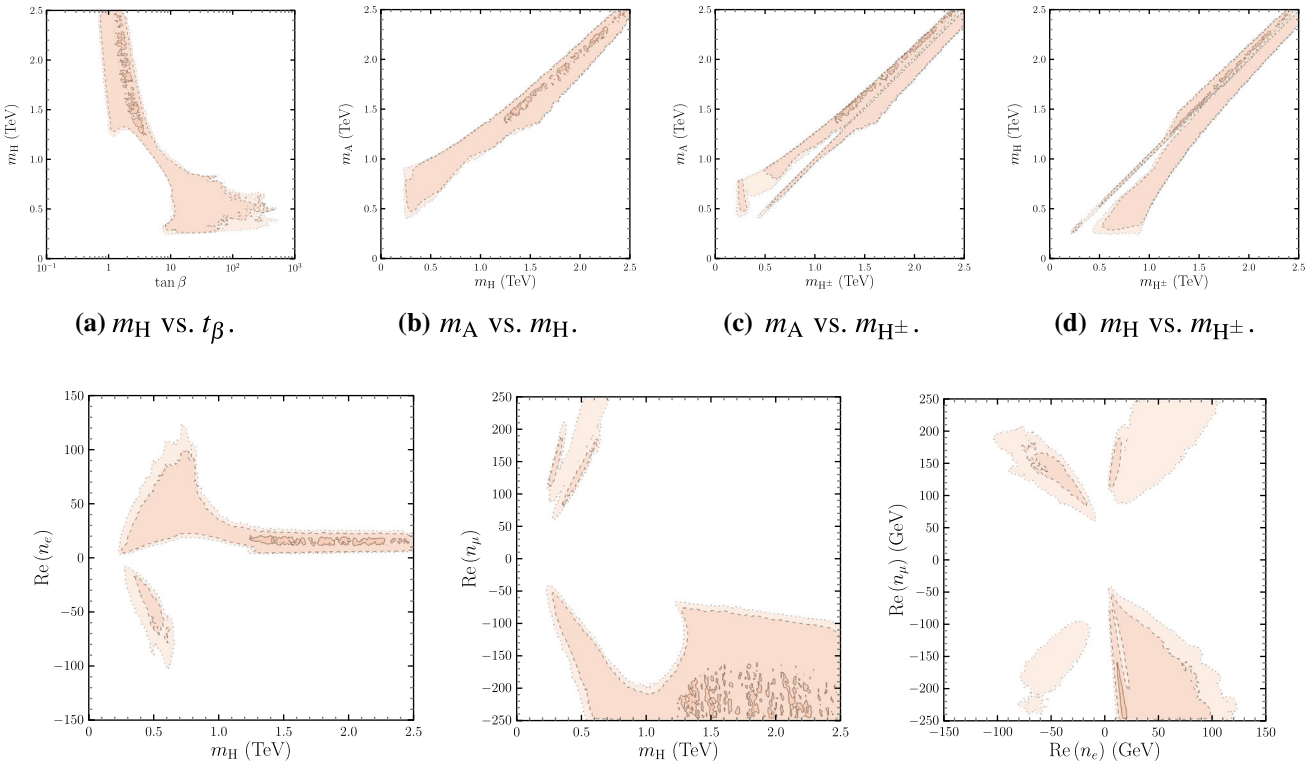

(a) m_{H} vs. t_β. **(b)** m_{A} vs. m_{H}. **(c)** m_{A} vs. $m_{\text{H}^\pm}$. **(d)** m_{H} vs. $m_{\text{H}^\pm}$.

(e) Re (n_e) vs. m_{H}. **(f)** Re (n_μ) vs. m_{H}. **(g)** Re (n_μ) vs. Re (n_e).

Fig. 15 Results with $(\Delta S, \Delta T)$ in Eq. (23), "conservative" case in [103]

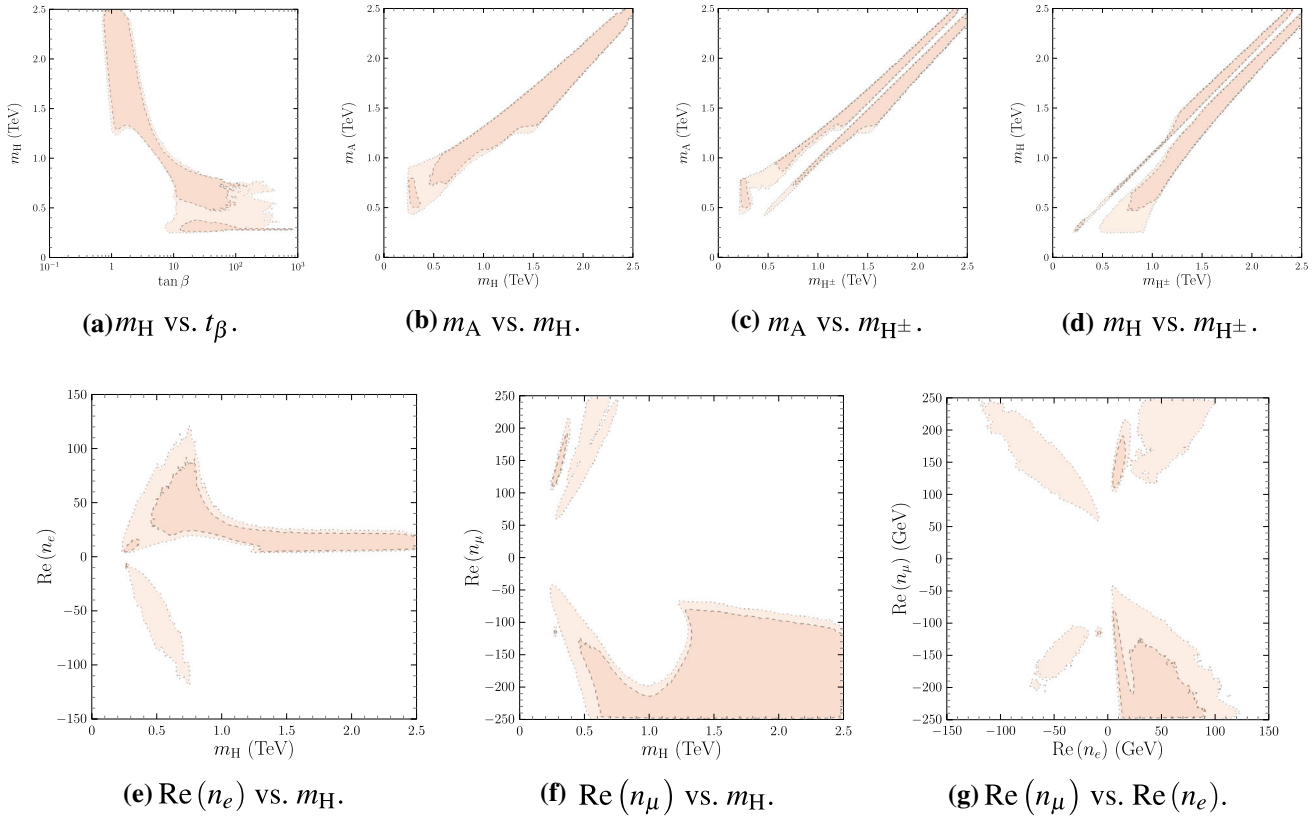

(a) $m_{\rm H}$ vs. t_β. **(b)** $m_{\rm A}$ vs. $m_{\rm H}$. **(c)** $m_{\rm A}$ vs. $m_{\rm H^\pm}$. **(d)** $m_{\rm H}$ vs. $m_{\rm H^\pm}$.

(e) $\mathrm{Re}\,(n_e)$ vs. $m_{\rm H}$. **(f)** $\mathrm{Re}\,(n_\mu)$ vs. $m_{\rm H}$. **(g)** $\mathrm{Re}\,(n_\mu)$ vs. $\mathrm{Re}\,(n_e)$.

Fig. 16 Results with $(\Delta S, \Delta T)$ in Eq. (24), from [104]

discussed in Sect. 3 that Eqs. (23) or (24) require, and the need of near degenerate scalars that the perturbativity requirements on the scalar potential impose for new scalar masses much larger than v.

– Overall agreement with the imposed constraints is worse in several regions in Figs. 15 and 16 than it was in the analyses of Sect. 6.2 (Figs. 8, 9 and 11). This is more dramatic in Fig. 16, where the agreement with constraints is worse than in Fig. 15 to the point that several regions are beyond the represented contour levels.

Despite these changes, the main characteristics of the allowed regions discussed in the previous sections still apply and are clearly identified in both Figs. 15 and 16.

Finally, since the oblique parameters S and T play an important role, Fig. 17 shows allowed regions for ΔS vs. ΔT in the two scenarios considered for the CDF M_W "explanation", together with the imposed $(\Delta T, \Delta S)$ constraint in each case. As anticipated, the constraint in Eq. (24) appears to be more difficult to accommodate than the constraint in Eq. (23). In fact, despite the different position of the ellipses corresponding to the $(\Delta T, \Delta S)$ constraints in Fig. 17a, b, the allowed regions are quite similar in both cases, that is, the model appears to be unable to accommodate values $\Delta T > 0.22$ together with $\Delta S > 0.02$. Other possible explanations of the CDF M_W anomaly have been addressed in [148–155].

6.5 Example points

In this section, some example points of the allowed parameter space are presented in order to specify the behavior pointed out in the previous plots. For the sake of clarity, we only focus on the analysis with "$a_e^{\rm Cs}$" concerning the electron anomaly: other cases do not change substantially beyond the differences already mentioned in Sect. 6.3.

From Table 1, it is clear that points 1–2 correspond to the solution with small values of t_β and large scalar masses: all scalars are above 1.2 TeV and their mass differences do not exceed ± 200 GeV. In this region, both anomalies are explained at two loops through the top quark terms, as one can easily check in Tables 2 and 3, where all loop contributions are normalized to the total δa_ℓ in such a way that their sum must be 1. One may also notice that δa_μ receives a subdominant one loop contribution. The lepton couplings $\mathrm{Re}\,(n_e)$ and $\mathrm{Re}\,(n_\mu)$ have opposite sign and they roughly satisfy the linear relation in Eq. (45) for the Cs case.

Regarding the appearance of the intermediate values of the scalar masses and t_β previously commented in Sect. 6.2, our point 3 gives a perfect example of that behavior. It is impor-

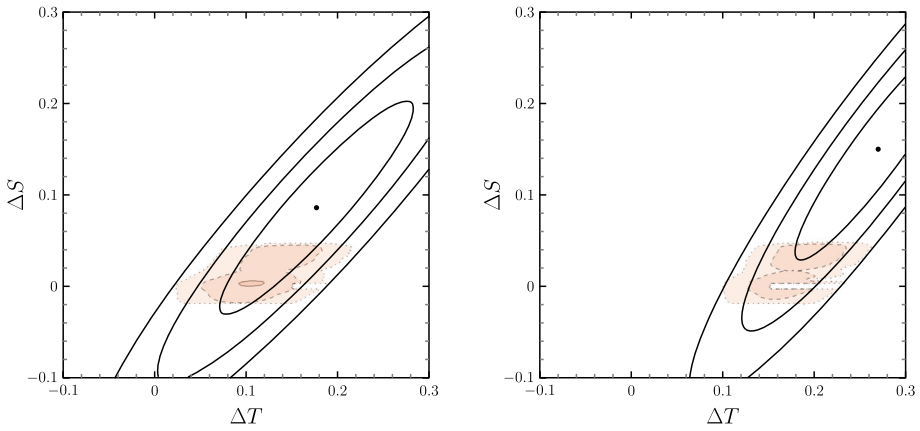

(a) $(\Delta S, \Delta T)$ in eq. (23). **(b)** $(\Delta S, \Delta T)$ in eq. (24).

Fig. 17 ΔS vs. ΔT, 1, 2 and 3σ 2D-$\Delta\chi^2$ contours from the imposed constraint are shown together with the allowed regions

Table 1 Example points, masses and Re (n_ℓ)'s in GeV

Point	m_{H}	m_{A}	$m_{\mathrm{H}^\pm}$	t_β	Re (n_e)	Re (n_μ)	Re (n_τ)
1	1351	1547	1560	1.34	6.08	−95.0	−40.79
2	1522	1567	1485	1.90	9.09	−158.9	126.5
3	1049	1322	1332	6.88	29.86	−245.0	−75.75
4	663	876	888	11.9	22.09	−172.9	224.6
5	621	938	946	21.5	54.26	238.1	−74.57
6	350	855	860	22.7	17.31	−87.22	94.99
7	372	815	362	34.6	25.44	−98.21	85.64
8	364	812	355	100	46.18	−95.14	79.90
9	360	810	352	186	−35.52	97.10	−119.2
10	1509	1604	1453	1.36	6.55	−112.8	70.7
11	508	809	834	89.3	38.85	−146.8	189.1

Table 2 Example points, δa_e values; columns 3 to 9 show the relative contributions of the different one and two loop terms to the value of δa_e in the second column

		1 loop			2 loop			
Point	δa_e	H	A	$\mathrm{H}^\pm$	$t\mathrm{H}$	$t\mathrm{A}$	$\tau\mathrm{H}$	$\tau\mathrm{A}$
1	−7.29	0	0	0	0.469	0.521	−0.012	0.011
2	−7.06	0	0	0	0.445	0.559	0.047	−0.051
3	−8.40	−0.001	0.001	0	0.524	0.526	−0.145	0.113
4	−7.53	−0.002	0.001	0	0.410	0.407	0.764	−0.554
5	−7.12	−0.016	0.007	0	0.627	0.541	−0.734	0.425
6	−6.96	−0.005	0.001	0	0.330	0.186	0.776	−0.207
7	−7.01	−0.009	0.002	0	0.300	0.187	0.926	−0.295
8	−8.41	−0.027	0.006	0	0.161	0.098	1.352	−0.419
9	−7.06	−0.019	0.004	0	−0.078	−0.049	1.879	−0.574
10	−7.06	0	0	0	0.453	0.548	0.019	−0.020
11	−7.09	−0.012	0.005	0	0.133	0.111	1.863	−0.996

Table 3 Example points, δa_μ values; columns 3 to 9 show the relative contributions of the different one and two loop terms to the value of δa_μ in the second column

		1 loop			2 loop			
Point	δa_μ	H	A	$H^\pm$	tH	tA	τH	τA
1	2.40	0.085	−0.063	−0.001	0.459	0.511	−0.012	0.011
2	2.58	0.177	−0.162	−0.003	0.439	0.553	0.046	−0.050
3	2.24	0.988	−0.614	−0.012	0.334	0.336	−0.093	0.072
4	2.31	1.124	−0.639	−0.013	0.216	0.215	0.403	−0.292
5	2.41	2.316	−1.024	−0.021	−0.169	−0.145	0.197	−0.114
6	2.51	0.870	−0.157	−0.003	0.095	0.054	0.224	−0.060
7	2.43	1.016	−0.224	−0.024	0.069	0.043	0.213	−0.068
8	2.21	1.093	−0.233	−0.025	0.026	0.016	0.219	−0.068
9	2.37	1.081	−0.227	−0.025	−0.013	−0.008	0.317	−0.097
10	2.54	0.092	−0.079	−0.002	0.448	0.542	0.019	−0.019
11	2.38	1.294	−0.518	−0.010	0.031	0.026	0.433	−0.231

tant to realize that large values of $|\mathrm{Re}\,(n_\mu)\,|$ are required in this region; in fact, they are almost reaching the perturbativity upper bound $|n_\ell| \leq 250$ GeV. On the other hand, although the top dominance still holds at two loops in the electron anomaly, the corresponding tau contributions begin to play a relevant role. This trend will continue as t_β grows and the quark contributions are more suppressed.

Finally, points 4–9 belong to the low mass region corresponding to a wide range of $t_\beta \gg 1$ values. As we have stressed before, two possible scenarios arise: one where $m_{\mathrm{H}^\pm} \simeq m_{\mathrm{A}}$ (points 4–6) and another where $m_{\mathrm{H}^\pm} \simeq m_{\mathrm{H}}$ (points 7–9). In all cases, the scalar masses are below 1 TeV and $m_{\mathrm{A}} > m_{\mathrm{H}}$, as anticipated. Taking into account the large values of t_β, the two loop contribution that dominates δa_e is generated by the tau loop. This confirms our expectation for $\mathrm{Re}\,(n_e)$: its sign is not fixed and it could be either positive or negative (point 9). Furthermore, in this region the muon anomaly is clearly one loop dominated, albeit there exists a subdominant contribution from the tau loop as well. This in turn means that $\mathrm{Re}\,(n_\mu)$ can take both signs, as one can easily check.

For completeness, the last two points have been included to give an example of the allowed parameter space in Sect. 6.4 considering the CDF M_W anomaly. It is clear that point 10 mimics the behavior of points 1–2, while point 11 presents the same features as points 4–6.

7 Conclusions

The experimental determinations of the muon and the electron anomalous magnetic moment point towards the necessity of lepton flavor non-universal New Physics. Aiming to address both leptonic anomalies simultaneously, we have considered a type I or type X 2HDM with a general flavor conserving lepton sector, one loop stable under renormalization, in which the new Yukawa couplings are completely decoupled from lepton mass proportionality. The latter turns out to be crucial in order to reproduce the $g-2$ muon anomaly together with the different scenarios one can consider for the $g-2$ electron anomaly, related to the Cs and/or the Rb recoil measurements of the fine structure constant. A thorough analysis of the parameter space of the model has been performed including all relevant theoretical and experimental constraints. The results show that the muon anomaly receives dominant one loop contributions for light new scalar masses in the 0.2–1.0 TeV range together with a significant hierarchy in the vacuum expectation values of the scalars, that is $t_\beta \gg 1$, while two loop Barr–Zee diagrams are also needed for heavy new scalars with masses above 1.2 TeV together with $t_\beta \sim 1$. On the other hand, the electron anomaly receives dominant two loop contributions in the whole range of scalar masses. Furthermore, we have analysed how the perturbativity assumptions on the lepton Yukawa couplings have direct impact on relevant physical observables: intermediate values of the scalar masses and t_β only arise when the perturbativity upper bound on n_ℓ reaches the electroweak scale. This might be relevant since we are entering an era of exclusion or discovery at the LHC, so that the allowed parameter space of the model must be fully scrutinized. The disagreement between the recent CDF measurement of M_W and the SM expectations for electroweak precision results can be translated into deviations $(\Delta S, \Delta T) \neq (0,0)$ of the oblique parameters. We have considered two different scenarios for $(\Delta S, \Delta T)$ values which "explain" the CDF disagreement. Both scenarios require a scalar spectrum where near degeneracies $m_{\mathrm{H}^\pm} \simeq m_{\mathrm{H}}$ or $m_{\mathrm{H}^\pm} \simeq m_{\mathrm{A}}$ are now disfavored, and where masses larger than 2 TeV are more difficult to accommodate.

However, concerning the n_ℓ couplings and t_β, the allowed regions have the same characteristics as in the analyses compatible with $(\Delta S, \Delta T) = (0, 0)$.

Acknowledgements The authors acknowledge support from Spanish *Agencia Estatal de Investigación-Ministerio de Ciencia e Innovación* (AEI-MICINN) under grants PID2019-106448GB-C33 and PID2020-113334GB-I00/AEI/10.13039/501100011033 (AEI/FEDER, UE) and from *Generalitat Valenciana* under grant PROMETEO 2019-113. The work of FCG is funded by MICINN, Spain (grant BES-2017-080070). CM is funded by *Conselleria de Innovación, Universidades, Ciencia y Sociedad Digital* from *Generalitat Valenciana* (grant ACIF/2021/284). MN is supported by the *GenT Plan* from *Generalitat Valenciana* under project CIDEGENT/2019/024.

Data Availability Statement This manuscript has no associated data or the data will not be deposited. [Authors' comment: All the data used in the analysis is publicly available in the references.]

Funded by SCOAP[3]. SCOAP[3] supports the goals of the International Year of Basic Sciences for Sustainable Development.

Appendices

A One loop stability under RGE

The evolution of the Yukawa couplings under one loop RGE [156–160] is given by:

$$\begin{aligned}\mathscr{D}Y_{d\alpha} &= a_d Y_{d\alpha} + \sum_{\rho=1}^{2} T^d_{\alpha,\rho} Y_{d\rho} \\ &+ \sum_{\rho=1}^{2}\Big(-2Y_{u\rho}Y^\dagger_{u\alpha}Y_{d\rho} + Y_{d\alpha}Y^\dagger_{d\rho}Y_{d\rho} \\ &+ \frac{1}{2}Y_{u\rho}Y^\dagger_{u\rho}Y_{d\alpha} + \frac{1}{2}Y_{d\rho}Y^\dagger_{d\rho}Y_{d\alpha}\Big) \\ &\text{with } T^d_{\alpha,\rho} \equiv 3\,\mathrm{Tr}\left(Y_{d\alpha}Y^\dagger_{d\rho} + Y^\dagger_{u\alpha}Y_{u\rho}\right) \\ &+ \mathrm{Tr}\left(Y_{\ell\alpha}Y^\dagger_{\ell\rho}\right), \end{aligned} \tag{58}$$

$$\begin{aligned}\mathscr{D}Y_{u\alpha} &= a_u Y_{u\alpha} + \sum_{\rho=1}^{2} T^u_{\alpha,\rho} Y_{u\rho} \\ &+ \sum_{\rho=1}^{2}\Big(-2Y_{d\rho}Y^\dagger_{d\alpha}Y_{u\rho} + Y_{u\alpha}Y^\dagger_{u\rho}Y_{u\rho} \\ &+ \frac{1}{2}Y_{d\rho}Y^\dagger_{d\rho}Y_{u\alpha} + \frac{1}{2}Y_{u\rho}Y^\dagger_{u\rho}Y_{u\alpha}\Big) \\ &\text{with } T^u_{\alpha,\rho} \equiv 3\,\mathrm{Tr}\left(Y_{u\alpha}Y^\dagger_{u\rho} + Y^\dagger_{d\alpha}Y_{d\rho}\right) \\ &+ \mathrm{Tr}\left(Y^\dagger_{\ell\alpha}Y_{\ell\rho}\right) = T^{d\,*}_{\alpha,\rho}, \end{aligned} \tag{59}$$

$$\begin{aligned}\mathscr{D}Y_{\ell\alpha} &= a_\ell Y_{\ell\alpha} + \sum_{\rho=1}^{2} T^\ell_{\alpha,\rho} Y_{\ell\rho} \\ &+ \sum_{\rho=1}^{2}\left(Y_{\ell\alpha}Y^\dagger_{\ell\rho}Y_{\ell\rho} + \frac{1}{2}Y_{\ell\rho}Y^\dagger_{\ell\rho}Y_{\ell\alpha}\right) \\ &\text{with } T^\ell_{\alpha,\rho} \equiv T^d_{\alpha,\rho}, \end{aligned} \tag{60}$$

where $\mathscr{D} \equiv 16\pi^2 \frac{d}{d\ln\mu}$, μ is the renormalization scale and

$$\begin{aligned} a_d &= -8g_c^2 - \frac{9}{4}g^2 - \frac{5}{12}g'^2, \qquad a_u = a_d - g'^2, \\ a_\ell &= -\frac{9}{4}g^2 - \frac{15}{4}g'^2, \end{aligned} \tag{61}$$

with g_c, g, g' the corresponding gauge coupling constants of $SU(3)_c$, $SU(2)_L$ and $U(1)_Y$, respectively.

The alignment condition in the quark sector

$$Y_{d2} = dY_{d1}, \tag{62}$$

$$Y_{u2} = uY_{u1}, \tag{63}$$

together with the existence of two unitary matrices $W_{L,R}$ in the lepton sector such that

$$L_i \equiv W_L^\dagger Y_{\ell i} W_R \tag{64}$$

are diagonal, guarantee the absence of SFCNC at tree level.

In order to ensure that Eqs. (62) and (63) in the quark sector hold at one loop, it is sufficient to impose [161]

$$\mathscr{D}Y_{d2} = \mathscr{D}(d)Y_{d1} + d\mathscr{D}Y_{d1}, \tag{65}$$

$$\mathscr{D}Y_{u2} = \mathscr{D}(u)Y_{u1} + u\mathscr{D}Y_{u1}, \tag{66}$$

or equivalently

$$\mathscr{D}Y_{d2} - d\mathscr{D}Y_{d1} = \mathscr{D}(d)Y_{d1} \propto Y_{d1}, \tag{67}$$

$$\mathscr{D}Y_{u2} - u\mathscr{D}Y_{u1} = \mathscr{D}(u)Y_{u1} \propto Y_{u1}, \tag{68}$$

where the proportionality constants are precisely the running of the parameters d and u in Eqs. (62) and (63). It is easy to check that

$$\begin{aligned}&\mathscr{D}Y_{d2} - d\mathscr{D}Y_{d1} \\ &= \Big\{3(u^* - d)(1 + ud)\mathrm{Tr}\left(Y^\dagger_{u1}Y_{u1}\right) \\ &\quad + \mathrm{Tr}\left((Y_{\ell 2} - dY_{\ell 1})(Y^\dagger_{\ell 1} + dY^\dagger_{\ell 2})\right)\Big\} Y_{d1} \\ &\quad + 2(d - u^*)(1 + ud)Y_{u1}Y^\dagger_{u1}Y_{d1}, \end{aligned} \tag{69}$$

$$\begin{aligned}&\mathscr{D}Y_{u2} - u\mathscr{D}Y_{u1}\\&= \left\{3(d^*-u)(1+ud)\mathrm{Tr}\left(Y_{d1}^\dagger Y_{d1}\right)\right.\\&\quad\left.+\mathrm{Tr}\left((Y_{\ell 2}^\dagger - uY_{\ell 1}^\dagger)(Y_{\ell 1}+uY_{\ell 2})\right)\right\}Y_{u1}\\&\quad+2(u-d^*)(1+ud)Y_{d1}Y_{d1}^\dagger Y_{u1}. \end{aligned} \tag{70}$$

Then we should have

$$(d-u^*)(1+ud)=0, \tag{71}$$

and, in particular, we are interested in the solution $d=u^*$. Therefore, the relation $\mathscr{D}(d)=\mathscr{D}(u^*)$ needs to be checked for the sake of consistency. Taking into account that, in our case,

$$\mathscr{D}(d) = \mathrm{Tr}\left((Y_{\ell 2} - dY_{\ell 1})(Y_{\ell 1}^\dagger + dY_{\ell 2}^\dagger)\right), \tag{72}$$

$$\mathscr{D}(u) = \mathrm{Tr}\left((Y_{\ell 2}^\dagger - uY_{\ell 1}^\dagger)(Y_{\ell 1} + uY_{\ell 2})\right), \tag{73}$$

it is clear that

$$\begin{aligned}\mathscr{D}(u)^* &= \mathrm{Tr}\left((Y_{\ell 1}^\dagger + u^*Y_{\ell 2}^\dagger)(Y_{\ell 2} - u^*Y_{\ell 1})\right)\\&= \mathrm{Tr}\left((Y_{\ell 2} - u^*Y_{\ell 1})(Y_{\ell 1}^\dagger + u^*Y_{\ell 2}^\dagger)\right)\\&= \mathrm{Tr}\left((Y_{\ell 2} - dY_{\ell 1})(Y_{\ell 1}^\dagger + dY_{\ell 2}^\dagger)\right) = \mathscr{D}(d),\end{aligned} \tag{74}$$

as it should. Hence, the quark sector is stable under RGE.

Concerning the lepton sector, one loop stability requires that

$$L_i + \mathscr{D}(L_i) \equiv W_L^\dagger(Y_{\ell i} + \mathscr{D}(Y_{\ell i}))W_R \tag{75}$$

remain simultaneously diagonal. In this sense, the only apparently problematic term in $\mathscr{D}(Y_{\ell i})$ has the structure $Y_{\ell a}Y_{\ell b}^\dagger Y_{\ell c}$, but

$$\begin{aligned}W_L^\dagger(Y_{\ell a}Y_{\ell b}^\dagger Y_{\ell c})W_R &= W_L^\dagger Y_{\ell a}W_R W_R^\dagger Y_{\ell b}^\dagger W_L W_L^\dagger Y_{\ell c}W_R\\&= L_a L_b^\dagger L_c,\end{aligned} \tag{76}$$

that is obviously diagonal [43]. Therefore, the lepton sector is also stable under RGE.

B δa_ℓ loops

B.1 One loop contributions

The interaction Lagrangian of neutral scalars S with charged leptons given by

$$\mathscr{L}_{S\ell\ell} = -\frac{m_\ell}{v}S\bar{\ell}(A_\ell^S + iB_\ell^S\gamma_5)\ell \tag{77}$$

generates the following one loop contribution to the anomalous magnetic moment of lepton ℓ

$$\delta a_\ell^{(1)} = \frac{1}{8\pi^2}\left(\frac{m_\ell}{v}\right)^2\sum_S\left\{[A_\ell^S]^2[2I_1(x_{\ell S}) - I_2(x_{\ell S})] - [B_\ell^S]^2 I_2(x_{\ell S})\right\}, \tag{78}$$

where $x_{\ell S}\equiv m_\ell^2/m_S^2$ and

$$I_1(x) = 1 + \frac{1-2x}{2x\sqrt{1-4x}}\ln\left(\frac{1+\sqrt{1-4x}}{1-\sqrt{1-4x}}\right) + \frac{1}{2x}\ln x, \tag{79}$$

$$\begin{aligned}I_2(x) &= \frac{1}{2} + \frac{1}{x} + \frac{1-3x}{2x^2\sqrt{1-4x}}\\&\quad\times\ln\left(\frac{1+\sqrt{1-4x}}{1-\sqrt{1-4x}}\right) + \frac{1-x}{2x^2}\ln x.\end{aligned} \tag{80}$$

Taking into account that in the limit $x \ll 1$

$$\begin{aligned}I_1(x) &\simeq x\left(-\frac{3}{2} - \ln x\right)\\&\quad + x^2\left(-\frac{16}{3} - 4\ln x\right) + \mathscr{O}(x^3),\end{aligned} \tag{81}$$

$$\begin{aligned}I_2(x) &\simeq x\left(-\frac{11}{6} - \ln x\right)\\&\quad + x^2\left(-\frac{89}{12} - 5\ln x\right) + \mathscr{O}(x^3),\end{aligned} \tag{82}$$

one can write for $m_\ell \ll m_S$

$$\begin{aligned}\delta a_\ell^{(1)} &= \frac{1}{8\pi^2}\left(\frac{m_\ell}{v}\right)^2\frac{m_\ell^2}{m_S^2}\left\{-[A_\ell^S]^2\left[\frac{7}{6} + \ln\left(\frac{m_\ell^2}{m_S^2}\right)\right]\right.\\&\quad\left.+[B_\ell^S]^2\left[\frac{11}{6} + \ln\left(\frac{m_\ell^2}{m_S^2}\right)\right]\right\}.\end{aligned} \tag{83}$$

On the other hand, the interaction Lagrangian of charged scalars $C^\pm$ with leptons written as

$$\mathscr{L}_{C\ell\nu} = -C^-\bar{\ell}(A_\ell^C + iB_\ell^C\gamma_5)\nu - C^+\bar{\nu}(A_\ell^{C*} + iB_\ell^{C*}\gamma_5)\ell, \tag{84}$$

gives rise to one loop contributions to the anomalous magnetic moment of lepton ℓ of the form

$$\delta a_\ell^{(1)} = -\frac{1}{8\pi^2}\sum_C\left\{|A_\ell^C|^2 + |B_\ell^C|^2\right\}I_3(x_{\ell C}), \tag{85}$$

with $x_{\ell C} = m_\ell^2/m_{C^\pm}^2$ and

$$I_3(x) = -\frac{1}{2} + \frac{1}{x} + \frac{1-x}{x^2}\ln(1-x). \tag{86}$$

For $x \ll 1$,

$$I_3(x) \simeq \frac{x}{6} + \frac{x^2}{12} + \mathscr{O}(x^3). \tag{87}$$

B.2 Two loop contributions

Together with Eq. (77), the interactions

$$\mathscr{L}_{S\bar{f}f} = -\frac{m_f}{v}S\bar{f}(\alpha_f^S + i\beta_f^S\gamma_5)f \tag{88}$$

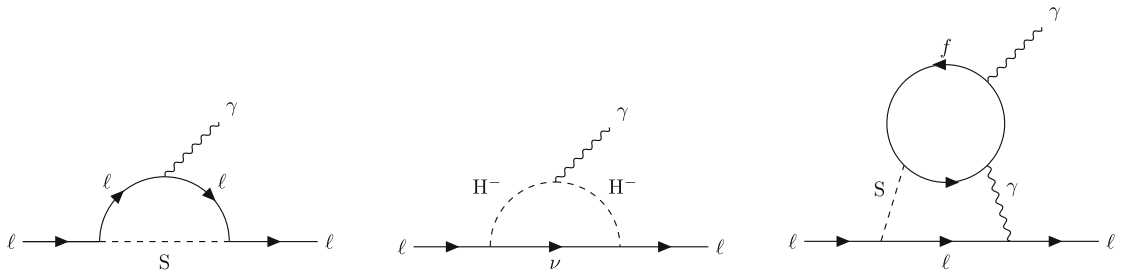

(a) Neutral mediated one loop contribution. **(b)** Charged mediated one loop contribution. **(c)** Barr-Zee two loop contribution.

Fig. 18 Illustrative one and two loop contributions to δa_ℓ

generate two loop Barr–Zee contributions to the anomalous magnetic moment of lepton ℓ:

$$\delta a_\ell^{(2)} = -\frac{2\alpha}{\pi}\frac{1}{8\pi^2}\left(\frac{m_\ell}{v}\right)^2 \sum_f \sum_S N_c^f Q_f^2 \times \left\{A_\ell^S \alpha_f^S f(z_{fS}) - B_\ell^S \beta_f^S g(z_{fS})\right\}, \quad (89)$$

where N_c^f and Q_f are the number of colours and the electric charge of the fermion running in the closed loop of Fig. 18c, respectively, and $z_{fS} = m_f^2/m_S^2$. The two loop functions $f(z)$ and $g(z)$ are

$$f(z) = \frac{z}{2}\int_0^1 dx\, \frac{1-2x(1-x)}{x(1-x)-z} \ln\left(\frac{x(1-x)}{z}\right), \quad (90)$$

$$g(z) = \frac{z}{2}\int_0^1 dx\, \frac{1}{x(1-x)-z} \ln\left(\frac{x(1-x)}{z}\right). \quad (91)$$

We refer to [162] to see other two loop contributions.

References

1. Muon g-2 Collaboration, G.W. Bennett et al., Final report of the muon E821 anomalous magnetic moment measurement at BNL. Phys. Rev. D **73**, 072003 (2006). arXiv:hep-ex/0602035
2. Muon g-2 Collaboration, B. Abi et al., Measurement of the positive muon anomalous magnetic moment to 0.46 ppm. Phys. Rev. Lett. **126**(14), 141801 (2021). arXiv:2104.03281
3. Muon g-2 Collaboration, T. Albahri et al., Measurement of the anomalous precession frequency of the muon in the Fermilab muon $g-2$ experiment. Phys. Rev. D **103**(7), 072002 (2021). arXiv:2104.03247
4. T. Aoyama et al., The anomalous magnetic moment of the muon in the Standard Model. Phys. Rep. **887**, 1–166 (2020). arXiv:2006.04822
5. T. Aoyama, M. Hayakawa, T. Kinoshita, M. Nio, Complete tenth-order QED contribution to the muon g-2. Phys. Rev. Lett. **109**, 111808 (2012). arXiv:1205.5370
6. T. Aoyama, T. Kinoshita, M. Nio, Theory of the anomalous magnetic moment of the electron. Atoms **7**, 28 (2019)
7. A. Czarnecki, W.J. Marciano, A. Vainshtein, Refinements in electroweak contributions to the muon anomalous magnetic moment. Phys. Rev. D **67**, 073006 (2003) [Erratum: Phys. Rev. D 73, 119901 (2006)]. arXiv:hep-ph/0212229
8. C. Gnendiger, D. Stöckinger, H. Stöckinger-Kim, The electroweak contributions to $(g-2)_\mu$ after the Higgs boson mass measurement. Phys. Rev. D **88**, 053005 (2013). arXiv:1306.5546
9. M. Davier, A. Hoecker, B. Malaescu, Z. Zhang, Reevaluation of the hadronic vacuum polarisation contributions to the Standard Model predictions of the muon $g-2$ and $\alpha(m_Z^2)$ using newest hadronic cross-section data. Eur. Phys. J. C **77**(12), 827 (2017). arXiv:1706.09436
10. A. Keshavarzi, D. Nomura, T. Teubner, Muon $g-2$ and $\alpha(M_Z^2)$: a new data-based analysis. Phys. Rev. D **97**(11), 114025 (2018). arXiv:1802.02995
11. G. Colangelo, M. Hoferichter, P. Stoffer, Two-pion contribution to hadronic vacuum polarization. JHEP **02**, 006 (2019). arXiv:1810.00007
12. M. Hoferichter, B.-L. Hoid, B. Kubis, Three-pion contribution to hadronic vacuum polarization. JHEP **08**, 137 (2019). arXiv:1907.01556
13. M. Davier, A. Hoecker, B. Malaescu, Z. Zhang, A new evaluation of the hadronic vacuum polarisation contributions to the muon anomalous magnetic moment and to $\alpha(m_Z^2)$. Eur. Phys. J. C **80**(3), 241 (2020) [Erratum: Eur. Phys. J. C 80, 410 (2020)]. arXiv:1908.00921
14. A. Keshavarzi, D. Nomura, T. Teubner, $g-2$ of charged leptons, $\alpha(M_Z^2)$, and the hyperfine splitting of muonium. Phys. Rev. D **101**(1), 014029 (2020). arXiv:1911.00367
15. A. Kurz, T. Liu, P. Marquard, M. Steinhauser, Hadronic contribution to the muon anomalous magnetic moment to next-to-next-to-leading order. Phys. Lett. B **734**, 144–147 (2014). arXiv:1403.6400
16. K. Melnikov, A. Vainshtein, Hadronic light-by-light scattering contribution to the muon anomalous magnetic moment revisited. Phys. Rev. D **70**, 113006 (2004). arXiv:hep-ph/0312226
17. P. Masjuan, P. Sanchez-Puertas, Pseudoscalar-pole contribution to the $(g_\mu - 2)$: a rational approach. Phys. Rev. D **95**(5), 054026 (2017). arXiv:1701.05829
18. G. Colangelo, M. Hoferichter, M. Procura, P. Stoffer, Dispersion relation for hadronic light-by-light scattering: two-pion contributions. JHEP **04**, 161 (2017). arXiv:1702.07347
19. M. Hoferichter, B.-L. Hoid, B. Kubis, S. Leupold, S.P. Schneider, Dispersion relation for hadronic light-by-light scattering: pion pole. JHEP **10**, 141 (2018). arXiv:1808.04823
20. A. Gérardin, H.B. Meyer, A. Nyffeler, Lattice calculation of the pion transition form factor with $N_f = 2+1$ Wilson quarks. Phys. Rev. D **100**(3), 034520 (2019). arXiv:1903.09471
21. J. Bijnens, N. Hermansson-Truedsson, A. Rodríguez-Sánchez, Short-distance constraints for the HLbL contribution to the muon anomalous magnetic moment. Phys. Lett. B **798**, 134994 (2019). arXiv:1908.03331

22. G. Colangelo, F. Hagelstein, M. Hoferichter, L. Laub, P. Stoffer, Longitudinal short-distance constraints for the hadronic light-by-light contribution to $(g-2)_\mu$ with large-N_c Regge models. JHEP **03**, 101 (2020). arXiv:1910.13432
23. T. Blum, N. Christ, M. Hayakawa, T. Izubuchi, L. Jin, C. Jung, C. Lehner, Hadronic light-by-light scattering contribution to the muon anomalous magnetic moment from lattice QCD. Phys. Rev. Lett. **124**(13), 132002 (2020). arXiv:1911.08123
24. G. Colangelo, M. Hoferichter, A. Nyffeler, M. Passera, P. Stoffer, Remarks on higher-order hadronic corrections to the muon g−2. Phys. Lett. B **735**, 90–91 (2014). arXiv:1403.7512
25. S. Borsanyi et al., Leading hadronic contribution to the muon magnetic moment from lattice QCD. Nature **593**(7857), 51–55 (2021). arXiv:2002.12347
26. M. Cè et al., Window observable for the hadronic vacuum polarization contribution to the muon $g-2$ from lattice QCD. arXiv:2206.06582
27. C. Alexandrou et al., Lattice calculation of the short and intermediate time-distance hadronic vacuum polarization contributions to the muon magnetic moment using twisted-mass fermions. arXiv:2206.15084
28. A. Crivellin, M. Hoferichter, C.A. Manzari, M. Montull, Hadronic vacuum polarization: $(g-2)_\mu$ versus global electroweak fits. Phys. Rev. Lett. **125**(9), 091801 (2020). arXiv:2003.04886
29. A. Keshavarzi, W.J. Marciano, M. Passera, A. Sirlin, Muon $g-2$ and $\Delta\alpha$ connection. Phys. Rev. D **102**(3), 033002 (2020). arXiv:2006.12666
30. G. Colangelo, M. Hoferichter, P. Stoffer, Constraints on the two-pion contribution to hadronic vacuum polarization. Phys. Lett. B **814**, 136073 (2021). arXiv:2010.07943
31. M. Passera, W.J. Marciano, A. Sirlin, The muon g-2 and the bounds on the Higgs boson mass. Phys. Rev. D **78**, 013009 (2008). arXiv:0804.1142
32. H. Davoudiasl, W.J. Marciano, Tale of two anomalies. Phys. Rev. D **98**(7), 075011 (2018). arXiv:1806.10252
33. T. Aoyama, M. Hayakawa, T. Kinoshita, M. Nio, Tenth-order QED contribution to the electron g-2 and an improved value of the fine structure constant. Phys. Rev. Lett. **109**, 111807 (2012). arXiv:1205.5368
34. S. Laporta, High-precision calculation of the 4-loop contribution to the electron g-2 in QED. Phys. Lett. B **772**, 232–238 (2017). arXiv:1704.06996
35. T. Aoyama, T. Kinoshita, M. Nio, Revised and improved value of the QED tenth-order electron anomalous magnetic moment. Phys. Rev. D **97**(3), 036001 (2018). arXiv:1712.06060
36. S. Volkov, Calculating the five-loop QED contribution to the electron anomalous magnetic moment: graphs without lepton loops. Phys. Rev. D **100**(9), 096004 (2019). arXiv:1909.08015
37. D. Hanneke, S. Fogwell, G. Gabrielse, New measurement of the electron magnetic moment and the fine structure constant. Phys. Rev. Lett. **100**, 120801 (2008). arXiv:0801.1134
38. E. Tiesinga, P.J. Mohr, D.B. Newell, B.N. Taylor, CODATA recommended values of the fundamental physical constants: 2018*. Rev. Mod. Phys. **93**(2), 025010 (2021)
39. R.H. Parker, C. Yu, W. Zhong, B. Estey, H. Müller, Measurement of the fine-structure constant as a test of the Standard Model. Science **360**, 191 (2018). arXiv:1812.04130
40. L. Morel, Z. Yao, P. Cladé, S. Guellati-Khélifa, Determination of the fine-structure constant with an accuracy of 81 parts per trillion. Nature **588**(7836), 61–65 (2020)
41. F.J. Botella, F. Cornet-Gomez, M. Nebot, Electron and muon $g-2$ anomalies in general flavour conserving two Higgs doublets models. Phys. Rev. D **102**(3), 035023 (2020). arXiv:2006.01934
42. A. Peñuelas, A. Pich, Flavour alignment in multi-Higgs-doublet models. JHEP **12**, 084 (2017). arXiv:1710.02040
43. F.J. Botella, F. Cornet-Gomez, M. Nebot, Flavor conservation in two-Higgs-doublet models. Phys. Rev. D **98**(3), 035046 (2018). arXiv:1803.08521
44. A. Broggio, E.J. Chun, M. Passera, K.M. Patel, S.K. Vempati, Limiting two-Higgs-doublet models. JHEP **11**, 058 (2014). arXiv:1409.3199
45. X.-F. Han, T. Li, L. Wang, Y. Zhang, Simple interpretations of lepton anomalies in the lepton-specific inert two-Higgs-doublet model. Phys. Rev. D **99**(9), 095034 (2019). arXiv:1812.02449
46. N. Haba, Y. Shimizu, T. Yamada, Muon and electron $g-2$ and the origin of the fermion mass hierarchy. PTEP **2020**(9), 093B05 (2020). arXiv:2002.10230
47. S. Jana, P.K. Vishnu, S. Saad, Resolving electron and muon $g-2$ within the 2HDM. Phys. Rev. D **101**(11), 115037 (2020). arXiv:2003.03386
48. B. Dutta, S. Ghosh, T. Li, Explaining $(g-2)_{\mu,e}$, the KOTO anomaly and the MiniBooNE excess in an extended Higgs model with sterile neutrinos. Phys. Rev. D **102**(5), 055017 (2020). arXiv:2006.01319
49. D. Sabatta, A.S. Cornell, A. Goyal, M. Kumar, B. Mellado, X. Ruan, Connecting muon anomalous magnetic moment and multilepton anomalies at LHC. Chin. Phys. C **44**(6), 063103 (2020). arXiv:1909.03969
50. E.J. Chun, T. Mondal, Explaining $g-2$ anomalies in two Higgs doublet model with vector-like leptons. JHEP **11**, 077 (2020). arXiv:2009.08314
51. S.-P. Li, X.-Q. Li, Y.-Y. Li, Y.-D. Yang, X. Zhang, Power-aligned 2HDM: a correlative perspective on $(g-2)_{e,\mu}$. JHEP **01**, 034 (2021). arXiv:2010.02799
52. L. Delle Rose, S. Khalil, S. Moretti, Explaining electron and muon $g-2$ anomalies in an aligned 2-Higgs Doublet Model with right-handed neutrinos. Phys. Lett. B **816**, 136216 (2021). arXiv:2012.06911
53. A.E.C. Hernández, S.F. King, H. Lee, Fermion mass hierarchies from vectorlike families with an extended 2HDM and a possible explanation for the electron and muon anomalous magnetic moments. Phys. Rev. D **103**(11), 115024 (2021). arXiv:2101.05819
54. W.-Y. Keung, D. Marfatia, P.-Y. Tseng, Axion-like particles, two-Higgs-doublet models, leptoquarks, and the electron and muon $g-2$. LHEP **2021**, 209 (2021). arXiv:2104.03341
55. X.-F. Han, T. Li, H.-X. Wang, L. Wang, Y. Zhang, Lepton-specific inert two-Higgs-doublet model confronted with the new results for muon and electron g-2 anomalies and multilepton searches at the LHC. Phys. Rev. D **104**(11), 115001 (2021). arXiv:2104.03227
56. A.E.C. Hernández, S. Kovalenko, M. Maniatis, I. Schmidt, Fermion mass hierarchy and g − 2 anomalies in an extended 3HDM Model. JHEP **10**, 036 (2021). arXiv:2104.07047
57. A. Jueid, J. Kim, S. Lee, J. Song, Type-X two-Higgs-doublet model in light of the muon g-2: confronting Higgs boson and collider data. Phys. Rev. D **104**(9), 095008 (2021). arXiv:2104.10175
58. A.E. Cárcamo Hernández, C. Espinoza, J. Carlos Gómez-Izquierdo, M. Mondragón, Fermion masses and mixings, dark matter, leptogenesis and $g-2$ muon anomaly in an extended 2HDM with inverse seesaw. arXiv:2104.02730
59. B. De, D. Das, M. Mitra, N. Sahoo, Magnetic moments of leptons, charged lepton flavor violations and dark matter phenomenology of a minimal radiative Dirac neutrino mass model. JHEP **08**, 202 (2022). arXiv:2106.00979
60. H. Bharadwaj, S. Dutta, A. Goyal, Leptonic g − 2 anomaly in an extended Higgs sector with vector-like leptons. JHEP **11**, 056 (2021). arXiv:2109.02586
61. L.T. Hue, A.E. Cárcamo Hernández, H.N. Long, T.T. Hong, Heavy singly charged Higgs bosons and inverse seesaw neutrinos as origins of large $(g-2)_{e,\mu}$ in two Higgs doublet models. arXiv:2110.01356

62. R.K. Barman, R. Dcruz, A. Thapa, Neutrino masses and magnetic moments of electron and muon in the Zee Model. JHEP **03**, 183 (2022). arXiv:2112.04523
63. J. Liu, C.E.M. Wagner, X.-P. Wang, A light complex scalar for the electron and muon anomalous magnetic moments. JHEP **03**, 008 (2019). arXiv:1810.11028
64. G. Hiller, C. Hormigos-Feliu, D.F. Litim, T. Steudtner, Anomalous magnetic moments from asymptotic safety. Phys. Rev. D **102**(7), 071901 (2020). arXiv:1910.14062
65. M. Endo, S. Iguro, T. Kitahara, Probing $e\mu$ flavor-violating ALP at Belle II. JHEP **06**, 040 (2020). arXiv:2002.05948
66. C. Hati, J. Kriewald, J. Orloff, A.M. Teixeira, Anomalies in ^{8}Be nuclear transitions and $(g-2)_{e,\mu}$: towards a minimal combined explanation. JHEP **07**, 235 (2020). arXiv:2005.00028
67. C.-K. Chua, Data-driven study of the implications of anomalous magnetic moments and lepton flavor violating processes of e, μ and τ. Phys. Rev. D **102**(5), 055022 (2020). arXiv:2004.11031
68. C. Arbeláez, R. Cepedello, R.M. Fonseca, M. Hirsch, $(g-2)$ anomalies and neutrino mass. Phys. Rev. D **102**(7), 075005 (2020). arXiv:2007.11007
69. P. Escribano, A. Vicente, Ultralight scalars in leptonic observables. JHEP **03**, 240 (2021). arXiv:2008.01099
70. S. Jana, P.K. Vishnu, W. Rodejohann, S. Saad, Dark matter assisted lepton anomalous magnetic moments and neutrino masses. Phys. Rev. D **102**(7), 075003 (2020). arXiv:2008.02377
71. N. Chen, B. Wang, C.-Y. Yao, The collider tests of a leptophilic scalar for the anomalous magnetic moments. arXiv:2102.05619
72. A. Biswas, S. Khan, $(g-2)_{e,\mu}$ and strongly interacting dark matter with collider implications. JHEP **07**, 037 (2022). arXiv:2112.08393
73. T.A. Chowdhury, M. Ehsanuzzaman, S. Saad, Dark matter and $(g-2)_{\mu,e}$ in radiative Dirac neutrino mass models. arXiv:2203.14983
74. M. Endo, W. Yin, Explaining electron and muon $g-2$ anomaly in SUSY without lepton-flavor mixings. JHEP **08**, 122 (2019). arXiv:1906.08768
75. M. Badziak, K. Sakurai, Explanation of electron and muon g $-$ 2 anomalies in the MSSM. JHEP **10**, 024 (2019). arXiv:1908.03607
76. J. Cao, Y. He, J. Lian, D. Zhang, P. Zhu, Electron and muon anomalous magnetic moments in the inverse seesaw extended NMSSM. Phys. Rev. D **104**(5), 055009 (2021). arXiv:2102.11355
77. S. Li, Y. Xiao, J.M. Yang, Can electron and muon $g-2$ anomalies be jointly explained in SUSY? Eur. Phys. J. C **82**(3), 276 (2022). arXiv:2107.04962
78. S. Li, Y. Xiao, J.M. Yang, Constraining CP-phases in SUSY: an interplay of muon/electron g$-$2 and electron EDM. Nucl. Phys. B **974**, 115629 (2022). arXiv:2108.00359
79. M. Bauer, M. Neubert, S. Renner, M. Schnubel, A. Thamm, Axionlike particles, lepton-flavor violation, and a new explanation of a_μ and a_e. Phys. Rev. Lett. **124**(21), 211803 (2020). arXiv:1908.00008
80. A.E. Cárcamo Hernández, Y. Hidalgo Velásquez, S. Kovalenko, H.N. Long, N.A. Pérez-Julve, V.V. Vien, Fermion spectrum and $g-2$ anomalies in a low scale 3-3-1 model. Eur. Phys. J. C **81**(2), 191 (2021). arXiv:2002.07347
81. I. Bigaran, R.R. Volkas, Getting chirality right: single scalar leptoquark solutions to the $(g-2)_{e,\mu}$ puzzle. Phys. Rev. D **102**(7), 075037 (2020). arXiv:2002.12544
82. L. Calibbi, M.L. López-Ibáñez, A. Melis, O. Vives, Muon and electron $g-2$ and lepton masses in flavor models. JHEP **06**, 087 (2020). arXiv:2003.06633
83. C.-H. Chen, T. Nomura, Electron and muon $g-2$, radiative neutrino mass, and $\ell' \to \ell\gamma$ in a $U(1)_{e-\mu}$ model. Nucl. Phys. B **964**, 115314 (2021). arXiv:2003.07638
84. I. Doršner, S. Fajfer, S. Saad, $\mu \to e\gamma$ selecting scalar leptoquark solutions for the $(g-2)_{e,\mu}$ puzzles. Phys. Rev. D **102**(7), 075007 (2020). arXiv:2006.11624
85. A. Bodas, R. Coy, S.J.D. King, Solving the electron and muon $g-2$ anomalies in Z' models. Eur. Phys. J. C **81**(12), 1065 (2021). arXiv:2102.07781
86. S. Fajfer, J.F. Kamenik, M. Tammaro, Interplay of new physics effects in $(g-2)_\ell$ and $h \to \ell^+\ell^-$—lessons from SMEFT. JHEP **06**, 099 (2021). arXiv:2103.10859
87. H.M. Lee, Leptoquark option for B-meson anomalies and leptonic signatures. Phys. Rev. D **104**(1), 015007 (2021). arXiv:2104.02982
88. B. Bhattacharya, A. Datta, D. Marfatia, S. Nandi, J. Waite, Axion-like particles resolve the $B \to \pi K$ and $g-2$ anomalies. Phys. Rev. D **104**(5), 051701 (2021). arXiv:2104.03947
89. M. Cadeddu, N. Cargioli, F. Dordei, C. Giunti, E. Picciau, Muon and electron g-2 and proton and cesium weak charges implications on dark Zd models. Phys. Rev. D **104**(1), 011701 (2021). arXiv:2104.03280
90. D. Borah, M. Dutta, S. Mahapatra, N. Sahu, Lepton anomalous magnetic moment with singlet-doublet fermion dark matter in a scotogenic U(1)Lμ-Lτ model. Phys. Rev. D **105**(1), 015029 (2022). arXiv:2109.02699
91. I. Bigaran, R.R. Volkas, Reflecting on chirality: CP-violating extensions of the single scalar-leptoquark solutions for the (g-2)e,μ puzzles and their implications for lepton EDMs. Phys. Rev. D **105**(1), 015002 (2022). arXiv:2110.03707
92. L.T. Hue, K.H. Phan, T.P. Nguyen, H.N. Long, H.T. Hung, An explanation of experimental data of $(g-2)_{e,\mu}$ in 3-3-1 models with inverse seesaw neutrinos. Eur. Phys. J. C **82**(8), 722 (2022). arXiv:2109.06089
93. H. Li, P. Wang, Solution of lepton g-2 anomalies with nonlocal QED. arXiv:2112.02971
94. J. Julio, S. Saad, A. Thapa, A tale of flavor anomalies and the origin of neutrino mass. arXiv:2202.10479
95. J. Julio, S. Saad, A. Thapa, Marriage between neutrino mass and flavor anomalies. arXiv:2203.15499
96. CDF Collaboration, T. Aaltonen et al., High-precision measurement of the W boson mass with the CDF II detector. Science **376**(6589), 170–176 (2022)
97. Particle Data Group Collaboration, P.A. Zyla et al., Review of Particle Physics. PTEP **2020**(8), 083C01 (2020)
98. H. Georgi, D. Nanopoulos, Suppression of flavor changing effects from neutral spinless meson exchange in gauge theories. Phys. Lett. B **82**(1), 95–96 (1979)
99. J.F. Donoghue, L.-F. Li, Properties of charged Higgs bosons. Phys. Rev. D **19**, 945–955 (1979)
100. F.J. Botella, J.P. Silva, Jarlskog-like invariants for theories with scalars and fermions. Phys. Rev. D **51**, 3870–3875 (1995)
101. ACME Collaboration, V. Andreev et al., Improved limit on the electric dipole moment of the electron. Nature **562**(7727), 355–360 (2018)
102. W. Grimus, L. Lavoura, O.M. Ogreid, P. Osland, The oblique parameters in multi-Higgs-doublet models. Nucl. Phys. B **801**, 81–96 (2008). arXiv:0802.4353
103. J. de Blas, M. Pierini, L. Reina, L. Silvestrini, Impact of the recent measurements of the top-quark and W-boson masses on electroweak precision fits. arXiv:2204.04204
104. C.-T. Lu, L. Wu, Y. Wu, B. Zhu, Electroweak precision fit and new physics in light of the W boson mass. Phys. Rev. D **106**(3), 035034 (2022). arXiv:2204.03796
105. M. Misiak et al., Estimate of $\mathscr{B}(\bar{B} \to X_s\gamma)$ at $O(\alpha_s^2)$. Phys. Rev. Lett. **98**, 022002 (2007). arXiv:hep-ph/0609232
106. A. Crivellin, A. Kokulu, C. Greub, Flavor-phenomenology of two-Higgs-doublet models with generic Yukawa structure. Phys. Rev. D **87**(9), 094031 (2013). arXiv:1303.5877

107. F.J. Botella, G.C. Branco, A. Carmona, M. Nebot, L. Pedro, M.N. Rebelo, Physical constraints on a class of two-Higgs doublet models with FCNC at tree level. JHEP **07**, 078 (2014). arXiv:1401.6147
108. S. Kanemura, T. Kubota, E. Takasugi, Lee–Quigg–Thacker bounds for Higgs boson masses in a two doublet model. Phys. Lett. B **313**, 155–160 (1993). arXiv:hep-ph/9303263
109. A.G. Akeroyd, A. Arhrib, E.-M. Naimi, Note on tree level unitarity in the general two Higgs doublet model. Phys. Lett. B **490**, 119–124 (2000). arXiv:hep-ph/0006035
110. I.F. Ginzburg, I.P. Ivanov, Tree-level unitarity constraints in the most general 2HDM. Phys. Rev. D **72**, 115010 (2005). arXiv:hep-ph/0508020
111. J. Horejsi, M. Kladiva, Tree-unitarity bounds for THDM Higgs masses revisited. Eur. Phys. J. C **46**, 81–91 (2006). arXiv:hep-ph/0510154
112. S. Kanemura, K. Yagyu, Unitarity bound in the most general two Higgs doublet model. Phys. Lett. B **751**, 289–296 (2015). arXiv:1509.06060
113. B. Grinstein, C.W. Murphy, P. Uttayarat, One-loop corrections to the perturbative unitarity bounds in the CP-conserving two-Higgs doublet model with a softly broken $\mathbb{Z}_2$ symmetry. JHEP **06**, 070 (2016). arXiv:1512.04567
114. M. Nebot, Bounded masses in two Higgs doublets models, spontaneous CP violation and $\mathbb{Z}_2$ symmetry. Phys. Rev. D **102**(11), 115002 (2020). arXiv:1911.02266
115. D. Das, New limits on tan β for 2HDMs with Z_2 symmetry. Int. J. Mod. Phys. A **30**(26), 1550158 (2015). arXiv:1501.02610
116. LHC Higgs Cross Section Working Group Collaboration, D. de Florian et al., Handbook of LHC Higgs cross sections: 4. Deciphering the nature of the Higgs sector. arXiv:1610.07922
117. R.V. Harlander, W.B. Kilgore, Next-to-next-to-leading order Higgs production at hadron colliders. Phys. Rev. Lett. **88**, 201801 (2002). arXiv:hep-ph/0201206
118. V. Ravindran, J. Smith, W.L. van Neerven, NNLO corrections to the total cross-section for Higgs boson production in hadron hadron collisions. Nucl. Phys. B **665**, 325–366 (2003). arXiv:hep-ph/0302135
119. A. Pak, M. Rogal, M. Steinhauser, Production of scalar and pseudo-scalar Higgs bosons to next-to-next-to-leading order at hadron colliders. JHEP **09**, 088 (2011). arXiv:1107.3391
120. R.V. Harlander, W.B. Kilgore, Production of a pseudoscalar Higgs boson at hadron colliders at next-to-next-to leading order. JHEP **10**, 017 (2002). arXiv:hep-ph/0208096
121. C. Anastasiou, K. Melnikov, Pseudoscalar Higgs boson production at hadron colliders in NNLO QCD. Phys. Rev. D **67**, 037501 (2003). arXiv:hep-ph/0208115
122. ALEPH Collaboration, S. Schael et al., Fermion pair production in e^+e^- collisions at 189–209-GeV and constraints on physics beyond the standard model. Eur. Phys. J. C **49**, 411–437 (2007). arXiv:hep-ex/0609051
123. I.P. Ivanov, J.P. Silva, Tree-level metastability bounds for the most general two Higgs doublet model. Phys. Rev. D **92**(5), 055017 (2015). arXiv:1507.05100
124. ATLAS Collaboration, G. Aad et al., Measurements of Higgs bosons decaying to bottom quarks from vector boson fusion production with the ATLAS experiment at $\sqrt{s} = 13$ TeV. Eur. Phys. J. C **81**(6), 537 (2021). arXiv:2011.08280
125. ATLAS Collaboration, G. Aad et al., Measurements of WH and ZH production in the $H \to b\bar{b}$ decay channel in pp collisions at 13 TeV with the ATLAS detector. Eur. Phys. J. C **81**(2), 178 (2021). arXiv:2007.02873
126. ATLAS Collaboration, Measurement of the Higgs boson decaying to b-quarks produced in association with a top-quark pair in pp collisions at $\sqrt{s} = 13$ TeV with the ATLAS detector
127. ATLAS Collaboration, Measurement of the properties of Higgs boson production at $\sqrt{s}$=13 TeV in the $H \to \gamma\gamma$ channel using 139 fb^{-1} of pp collision data with the ATLAS experiment
128. ATLAS Collaboration, G. Aad et al., A search for the dimuon decay of the Standard Model Higgs boson with the ATLAS detector. Phys. Lett. B **812**, 135980 (2021). arXiv:2007.07830
129. ATLAS Collaboration, A combination of measurements of Higgs boson production and decay using up to 139 fb^{-1} of proton–proton collision data at $\sqrt{s} = 13$ TeV collected with the ATLAS experiment
130. ATLAS Collaboration, G. Aad et al., Measurement of the production cross section for a Higgs boson in association with a vector boson in the $H \to WW^* \to \ell\nu\ell\nu$ channel in pp collisions at $\sqrt{s}$ = 13 TeV with the ATLAS detector. Phys. Lett. B **798**, 134949 (2019). arXiv:1903.10052
131. ATLAS Collaboration, G. Aad et al., Higgs boson production cross-section measurements and their EFT interpretation in the 4ℓ decay channel at $\sqrt{s}$ =13 TeV with the ATLAS detector. Eur. Phys. J. C **80**(10), 957 (2020) [Erratum: Eur. Phys. J. C 81, 29 (2021)]. arXiv:2004.03447]
132. CMS Collaboration, VBF H to bb using the 2015 data sample
133. CMS Collaboration, Combined Higgs boson production and decay measurements with up to 137 fb^{-1} of proton–proton collision data at $\sqrt{s}$ = 13 TeV
134. CMS Collaboration, A.M. Sirunyan et al., Evidence for Higgs boson decay to a pair of muons. JHEP **01**, 148 (2021). arXiv:2009.04363
135. CMS Collaboration, A.M. Sirunyan et al., Measurements of Higgs boson production cross sections and couplings in the diphoton decay channel at $\sqrt{s}$ = 13 TeV. JHEP **07**, 027 (2021). arXiv:2103.06956
136. CMS Collaboration, A.M. Sirunyan et al., Measurements of production cross sections of the Higgs boson in the four-lepton final state in proton–proton collisions at $\sqrt{s} = 13$ TeV. Eur. Phys. J. C **81**(6), 488 (2021). arXiv:2103.04956
137. V. Cirigliano, I. Rosell, Two-loop effective theory analysis of pi (K) –> e anti-nu/e [gamma] branching ratios. Phys. Rev. Lett. **99**, 231801 (2007). arXiv:0707.3439
138. A. Pich, Precision tau physics. Prog. Part. Nucl. Phys. **75**, 41–85 (2014). arXiv:1310.7922
139. ATLAS Collaboration, M. Aaboud et al., Search for new high-mass phenomena in the dilepton final state using 36 fb^{-1} of proton–proton collision data at $\sqrt{s} = 13$ TeV with the ATLAS detector. JHEP **10**, 182 (2017). arXiv:1707.02424
140. CMS Collaboration, A.M. Sirunyan et al., Search for MSSM Higgs bosons decaying to $\mu + \mu -$ in proton–proton collisions at s=13TeV. Phys. Lett. B **798**, 134992 (2019). arXiv:1907.03152
141. ATLAS Collaboration, M. Aaboud et al., Search for additional heavy neutral Higgs and gauge bosons in the ditau final state produced in 36 fb^{-1} of pp collisions at $\sqrt{s} = 13$ TeV with the ATLAS detector. JHEP **01**, 055 (2018). arXiv:1709.07242
142. CMS Collaboration, V. Khachatryan et al., Search for heavy resonances decaying to tau lepton pairs in proton–proton collisions at $\sqrt{s} = 13$ TeV. JHEP **02**, 048 (2017). arXiv:1611.06594
143. CMS Collaboration, A.M. Sirunyan et al., Search for additional neutral MSSM Higgs bosons in the $\tau\tau$ final state in proton–proton collisions at $\sqrt{s} = 13$ TeV. JHEP **09**, 007 (2018). arXiv:1803.06553
144. ATLAS Collaboration, M. Aaboud et al., Search for charged Higgs bosons decaying into top and bottom quarks at $\sqrt{s}$ = 13 TeV with the ATLAS detector. JHEP **11**, 085 (2018). arXiv:1808.03599
145. CMS Collaboration, A.M. Sirunyan et al., Search for charged Higgs bosons in the $H^{\pm} \to \tau^{\pm}\nu_{\tau}$ decay channel in proton-proton collisions at $\sqrt{s} = 13$ TeV. JHEP **07**, 142 (2019). arXiv:1903.04560

146. CMS Collaboration, A.M. Sirunyan et al., Search for a charged Higgs boson decaying into top and bottom quarks in events with electrons or muons in proton-proton collisions at $\sqrt{s}$ = 13 TeV. JHEP **01**, 096 (2020). arXiv:1908.09206
147. CMS Collaboration, A.M. Sirunyan et al., Search for charged Higgs bosons decaying into a top and a bottom quark in the all-jet final state of pp collisions at $\sqrt{s}$ = 13 TeV. JHEP **07**, 126 (2020). arXiv:2001.07763
148. Y.-Z. Fan, T.-P. Tang, Y.-L.S. Tsai, L. Wu, Inert Higgs dark matter for CDF II W-boson mass and detection prospects. Phys. Rev. Lett. **129**(9), 091802 (2022). arXiv:2204.03693
149. T.-P. Tang, M. Abdughani, L. Feng, Y.-L.S. Tsai, J. Wu, Y.-Z. Fan, NMSSM neutralino dark matter for W-boson mass and muon $g-2$ and the promising prospect of direct detection. arXiv:2204.04356
150. Y.H. Ahn, S.K. Kang, R. Ramos, Implications of new CDF-II W boson mass on two Higgs doublet model. arXiv:2204.06485
151. X.-F. Han, F. Wang, L. Wang, J.M. Yang, Y. Zhang, A joint explanation of W-mass and muon g-2 in 2HDM. arXiv:2204.06505
152. T.A. Chowdhury, J. Heeck, S. Saad, A. Thapa, W boson mass shift and muon magnetic moment in the Zee model. Phys. Rev. D **106**(3), 035004 (2022). arXiv:2204.08390
153. K. Ghorbani, P. Ghorbani, W-Boson mass anomaly from scale invariant 2HDM. arXiv:2204.09001
154. S. Baek, Implications of CDF W-mass and $(g-2)_\mu$ on $U(1)_{L_\mu - L_\tau}$ model. arXiv:2204.09585
155. S. Baek, Implications of CDF W-mass and $(g-2)_\mu$ on $U(1)_{L_\mu - L_\tau}$ model. arXiv:2204.09585
156. G. Cvetic, S.S. Hwang, C.S. Kim, One loop renormalization group equations of the general framework with two Higgs doublets. Int. J. Mod. Phys. A **14**, 769–798 (1999). arXiv:hep-ph/9706323
157. G. Cvetič, S.S. Hwang, C.S. Kim, Higgs-mediated flavor-changing neutral currents in the general framework with two Higgs doublets: an RGE analysis. Phys. Rev. D **58**, 116003 (1998)
158. P.M. Ferreira, L. Lavoura, J.P. Silva, Renormalization-group constraints on Yukawa alignment in multi-Higgs-doublet models. Phys. Lett. B **688**, 341–344 (2010). arXiv:1001.2561
159. W. Grimus, L. Lavoura, Renormalization of the neutrino mass operators in the multi-Higgs-doublet standard model. Eur. Phys. J. C **39**, 219–227 (2005). arXiv:hep-ph/0409231
160. T.P. Cheng, E. Eichten, L.-F. Li, Higgs phenomena in asymptotically free gauge theories. Phys. Rev. D **9**, 2259–2273 (1974)
161. F.J. Botella, G.C. Branco, A.M. Coutinho, M.N. Rebelo, J.I. Silva-Marcos, Natural quasi-alignment with two Higgs doublets and RGE stability. Eur. Phys. J. C **75**, 286 (2015). arXiv:1501.07435
162. A. Cherchiglia, P. Kneschke, D. Stöckinger, H. Stöckinger-Kim, The muon magnetic moment in the 2HDM: complete two-loop result. JHEP **01**, 007 (2017) [Erratum: JHEP 10, 242 (2021)]. arXiv:1607.06292